vehicles

MDPI

Article

Topology Design, Multi-Objective Optimization, and Dynamic Performance Evaluation of a PCM-Buffered SOFC-MGT Hybrid Powertrain for Heavy-Duty Trucks

Saeed Shirazi [1], Majid Ghassemi [1] and Mahmoud Chizari [2,*]

[1] School of Mechanical Engineering, KN Toosi University of Technology, Tehran 19967-15433, Iran
[2] School of Physics, Engineering and Computer Science, College Lane Campus, University of Hertfordshire, Hatfield AL10 9AB, UK
* Correspondence: m.chizari@herts.ac.uk

Abstract

Decarbonizing heavy-duty logistics requires powertrains that integrate novel topology design, degradation-aware optimization, and robust dynamic performance under real-world operational loads. While solid oxide fuel cells offer high efficiency, their application in transportation is hindered by thermal fatigue. This study proposes a novel hybrid powertrain topology integrating a metal-supported solid oxide fuel cell (SOFC), a micro gas turbine (MGT), and an aluminum–silicon phase change material (PCM) thermal buffer. A high-fidelity dynamic model is developed and coupled with a multi-objective optimization framework to size the PCM buffer and battery pack, balancing capital expenditure and system lifetime. Furthermore, a degradation-aware energy management strategy based on a thermal state-of-charge metric is introduced. Simulations over a 10 h dynamic drive cycle indicate that the optimal configuration (120 kg PCM, 80 kWh battery) extends the SOFC's simulated remaining useful life to 38,400 h, a 2.5-fold improvement over unbuffered systems. Concurrently, the proposed energy management strategy reduces the MGT mechanical wear index by 98% compared to conventional load-following strategies. The system demonstrates robust performance across ambient temperatures from −20 °C to +45 °C and achieves a 22% reduction in projected capital expenditure compared to standard proton exchange membrane fuel cell powertrains. This topology offers a highly durable and economically viable pathway for next-generation zero-emission heavy-duty vehicles. This work addresses a critical gap in the literature: the lack of integrated thermal buffering and degradation-aware control strategies for high-temperature fuel cell systems in dynamic vehicular applications. By coupling a physical latent heat buffer with a novel Thermal-SOC-proportional Energy Management Strategy, the proposed architecture directly targets the primary degradation mechanisms that have historically impeded SOFC commercialization in heavy-duty transport.

Keywords: solid oxide fuel cell (SOFC); phase change material (PCM); micro gas turbine (MGT); heavy-duty truck; thermal-SOC energy management; multi-objective optimization

Check for updates

Academic Editors: Yong Chen, Qin Li and Jie Li

Received: 28 April 2026
Revised: 12 June 2026
Accepted: 18 June 2026
Published: 27 June 2026

1. Introduction

The heavy-duty road freight sector is a primary contributor to global greenhouse gas emissions, making its decarbonization imperative for achieving international climate targets [1]. Recent assessments highlight the urgency of this transition: the Clean Hydrogen

JU Annual Work Programme 2025 emphasizes the accelerated deployment of hydrogen-based solutions for heavy-duty applications, while the IDTechEx FCEV 2025–2045 report projects a 60-fold market growth for fuel cell electric vehicles by 2045, driven by zero-emission mandates [2,3]. Similarly, the U.S. DOE medium- and heavy-duty vehicle plan outlines strategies to achieve 30% zero-emission heavy-duty vehicle sales by 2030, aligning with global efforts to reduce emissions from long-haul logistics [4].

In recent years, while battery electric vehicles (BEVs) have demonstrated zero-emission viability for short-haul urban logistics, their deployment in long-haul transit faces formidable technological and economic barriers [5]. The relatively low energy density of lithium-ion batteries necessitates the installation of massive battery packs, often weighing between 5 and 9 tons, which severely restricts the permissible cargo payload capacity of Class 8 trucks and undermines fleet profitability [6,7]. Furthermore, the rapid charging of these immense battery capacities demands megawatt-scale infrastructure, introducing profound challenges such as extended operational downtime, severe space capacity constraints at charging stations, and disruptive peak loads on the electrical distribution grid [8,9]. To circumvent the range and payload limitations inherent to battery-centric systems, fuel cell hybrid electric vehicles have emerged as a highly strategic alternative for heavy-duty transportation [10]. Among these, Proton Exchange Membrane Fuel Cells (PEMFC) currently dominate the commercial landscape due to their rapid cold-start capabilities [11]. Nevertheless, the integration of PEMFCs into heavy-duty trucks is fundamentally constrained by severe thermal management bottlenecks and inherent durability issues [12]. Operating at relatively low temperatures (typically 60–80 °C), PEMFCs exhibit a marginal temperature differential with the ambient environment. Consequently, rejecting the massive waste heat generated during uphill or high-load operations necessitates extraordinarily large radiators and cooling systems, imposing critical aerodynamic and packaging constraints on the vehicle chassis [13]. Additionally, the aggressive dynamic load cycling dictated by real-world driving conditions induces severe thermal shocks and rapid voltage degradation within the polymer membrane. This accelerated degradation significantly curtails the remaining useful life (RUL) of the stack, thereby rendering the total cost of ownership (TCO) economically prohibitive for freight operators [14,15].

To overcome the inherent thermal management bottlenecks of PEMFCs, solid oxide fuel cells (SOFCs) have emerged as a highly efficient alternative for heavy-duty powertrains. Operating at elevated temperatures (typically 600–800 °C), SOFCs facilitate high-grade waste heat recovery and exhibit superior tolerance to fuel impurities. Recent advancements in metal-supported SOFCs (MS-SOFCs) have significantly enhanced their mechanical robustness and power density, making them increasingly viable for demanding automotive applications [16–18]. For instance, Zhang et al. (2025) reviewed MS-SOFC applications in transportation, highlighting improved dynamic start-up performance compared to anode-supported designs [17], while Ren et al. (2025) compared the behaviours of anode-supported and metal-supported SOFCs during hot start-up, demonstrating the faster thermal response capabilities of MS configurations [18]. However, the deployment of SOFCs in highly dynamic environments, such as long-haul trucking, is fundamentally constrained by their susceptibility to thermal fatigue. Rapid load fluctuations, characteristic of real-world driving cycles involving steep gradients and frequent braking, inherently generate severe spatial temperature gradients within the stack. These thermal shocks accelerate irreversible degradation mechanisms, including nickel particle coarsening in the anode and flexural strength deterioration in the ceramic layers [19,20].

A widely explored strategy to maximize the system-level efficiency of high-temperature fuel cells is their integration with Micro Gas Turbines (MGTs) to recover exhaust heat [21]. While SOFC-MGT hybrid systems exhibit exceptional steady-state performance, their dynamic operation in vehicular applications introduces critical control conflicts. Conventional thermostatic (bang-bang) or aggressive load-following control strategies impose severe mechanical stress on MGT air foil bearings and induce thermal fatigue in the recuperator [22,23]. To effectively decouple the SOFC's thermal transients from the MGT's mechanical limitations, this study proposes a novel powertrain topology incorporating a high-temperature PCM, specifically a eutectic Al–Si alloy [24], as a latent heat buffer. While PCMs have been extensively studied for stationary energy storage [25], their integration into mobile SOFC-MGT architectures remains largely unexplored. Recent advances in metallic PCMs for SOFC thermal management include microencapsulated Al–Si alloys for high-temperature stability [26] and PCM-integrated stacks for operating range extension [27], demonstrating reduced thermal gradients and enhanced durability. By coupling this physical thermal buffer with an advanced Energy Management Strategy (EMS) [28], the control paradigm is shifted from rigid load-following to a continuous, thermal-state-of-charge (SOC_{th})-proportional modulation. This integrated approach aims to entirely dampen the destructive thermal gradients on the SOFC, minimize MGT mechanical wear, and significantly extend the system's remaining useful life (RUL) under realistic heavy-duty operations.

Despite the proven theoretical merits of PCMs in stationary high-temperature thermal energy storage, their dynamic integration into mobile SOFC-MGT hybrid powertrains remains a conspicuous gap in the literature. Previous studies have predominantly concentrated on steady-state part-load operations or employed conventional thermostatic control strategies. Furthermore, the simultaneous multi-objective sizing of the latent heat buffer and the electrical energy storage system, tightly coupled with a degradation-aware control logic, has not been comprehensively investigated to date [29,30]. The commercial deployment of SOFCs in heavy-duty transportation has been historically impeded by their vulnerability to thermal shocks and prolonged start-up times. Dynamic vehicular load fluctuations inherently induce severe thermal gradients, leading to mechanical degradation and micro-cracking of the ceramic electrolyte. Therefore, integrating a thermal buffering mechanism, such as a PCM, becomes physically imperative to decouple the transient electrical demands from the stack's thermal response, thereby unlocking the true potential of SOFCs for dynamic applications.

The aim of this study is to develop and rigorously evaluate a novel, degradation-aware hybrid powertrain topology tailored for Class 8 heavy-duty trucks, which seamlessly integrates a metal-supported SOFC, a micro gas turbine, a lithium-ion battery pack, and a high-temperature Al–Si eutectic PCM buffer. The specific objectives are threefold: first, to formulate a high-fidelity dynamic simulation framework that accurately captures the coupled electrochemical, thermodynamic, and mechanical domains of the proposed system; second, to employ the Non-dominated Sorting Genetic Algorithm II (NSGA-II) to resolve the techno-economic trade-off between capital expenditure and system degradation through optimal sizing of the PCM buffer and battery capacity; and third, to design and demonstrate a continuous, Thermal-SOC-proportional Energy Management Strategy that minimizes MGT mechanical wear and extends the projected remaining useful life of the SOFC stack under realistic long-haul drive cycles, thereby establishing the proposed architecture as a durable, economically viable, and robust paradigm for next-generation heavy-duty vehicles.

The present study is motivated by three interconnected gaps in the current literature: (i) the absence of high-temperature PCM integration strategies for mobile SOFC-MGT architectures, despite proven benefits in stationary thermal storage; (ii) the lack of degradation-aware control frameworks that explicitly link thermal buffering to component lifetime extension; and (iii) insufficient techno-economic analyses that simultaneously resolve

CAPEX, durability, and operational robustness for long-haul heavy-duty applications. To address these gaps, this work makes three specific contributions: first, a novel powertrain topology that physically decouples SOFC thermal transients from MGT mechanical constraints via an Al–Si eutectic PCM buffer; second, a continuous, Thermal-SOC-proportional Energy Management Strategy that minimizes mechanical wear and thermal fatigue through intelligent, state-based modulation; and third, a comprehensive NSGA-II multi-objective optimization framework that quantifies the trade-off between capital investment and projected stack lifetime. Collectively, these contributions establish a durable, economically viable, and climatically robust pathway for zero-emission heavy-duty freight logistics.

2. Materials and Methods

The integrated analytical framework for the proposed SOFC-MGT-PCM hybrid powertrain is illustrated in Figure 1. The workflow consists of six sequential stages: first, definition of vehicle specifications and drive cycle; second, high-fidelity dynamic modelling of all subsystems; third, multi-level validation using experimental and standard cycle data; fourth, NSGA-II optimization that balances capital expenditure against degradation; fifth, implementation of the Thermal-SOC Energy Management Strategy; and sixth, comprehensive dynamic simulation and comparative evaluation. The following subsections elaborate on each phase, presenting the governing equations, parameter sets, and computational protocols necessary for full reproducibility.

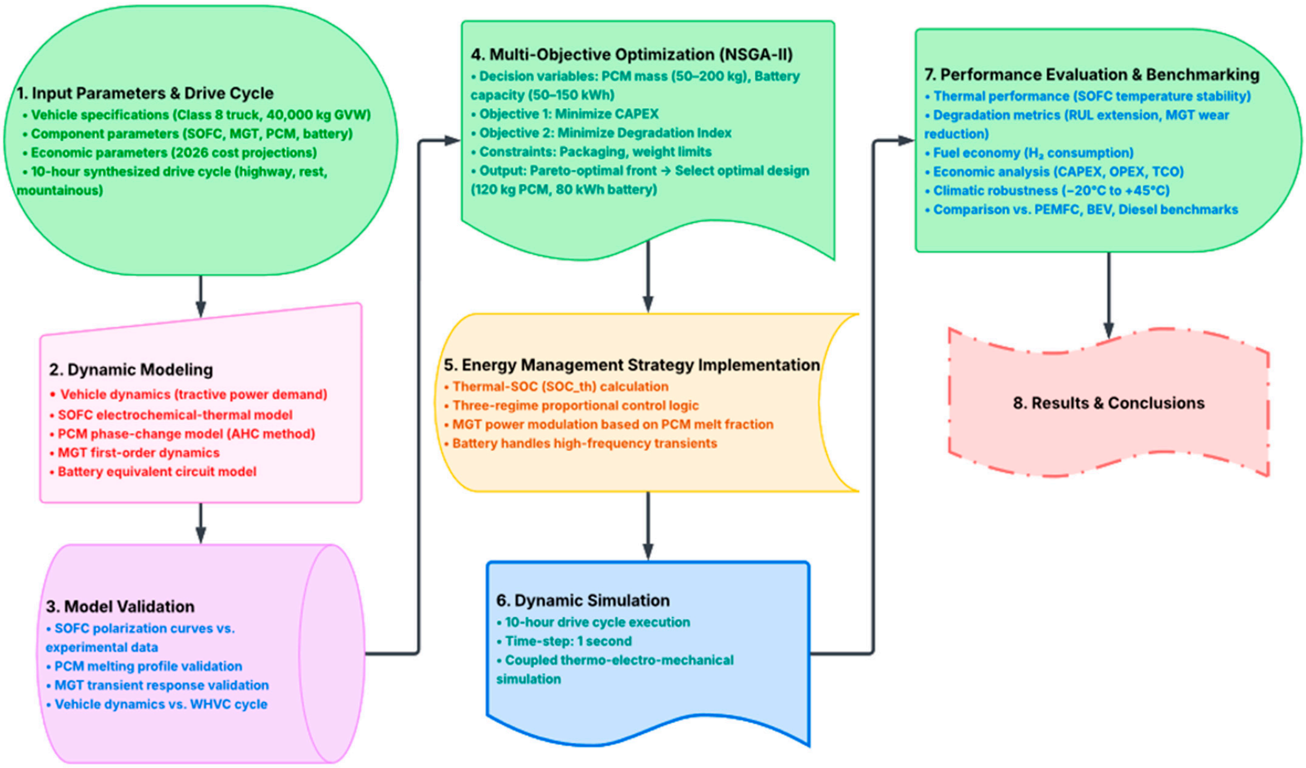

Figure 1. Flowchart of the complete analysis procedure employed in this study. The workflow encompasses: (i) specification of vehicle parameters, component models, and the synthesized 10 h drive cycle; (ii) high-fidelity dynamic modelling of the SOFC-MGT-PCM-battery hybrid powertrain; (iii) multi-tiered validation against experimental data and standard cycles; (iv) NSGA-II multi-objective optimization to determine Pareto-optimal PCM mass and battery capacity; (v) implementation of the Thermal-SOC-proportional Energy Management Strategy; (vi) dynamic simulation over the full drive cycle; and (vii) comprehensive performance evaluation including thermal stability, degradation mitigation, fuel economy, techno-economic analysis, and benchmarking against conventional powertrains.

2.1. Powertrain Architecture and Vehicle Dynamics Modelling

The hybrid powertrain architecture proposed in this study is meticulously designed to accommodate the transient load demands of a 40-ton Class 8 heavy-duty truck operating under long-haul conditions. To accurately quantify the instantaneous tractive power demand (P_{req}) at the wheels, a comprehensive longitudinal vehicle dynamics model is utilized, adopting established formulations from advanced vehicle propulsion and dynamics literature [31,32]. The system integrates four principal components that operate synergistically to optimize both electrical power dispatch and waste heat recovery. The required power is formulated as the dynamic equilibrium of aerodynamic drag, rolling resistance, road grading, and acceleration inertia:

$$P_{req}(t) = v(t)\cdot\left(M_{GVM}gC_{rr}cos(\theta) + M_{GVM}gsin(\theta) + \frac{1}{2}\rho A_f C_d v(t)^2 + M_{GVM}\frac{dv(t)}{dt}\right), \quad (1)$$

where $v(t)$ is the instantaneous velocity derived from the driving cycle, M_{GVM} is the gross vehicle mass (40,000 kg), C_{rr} represents the rolling resistance coefficient, θ is the road gradient angle, ρ denotes air density, A_f is the frontal area, and C_d is the aerodynamic drag coefficient. The electrical power balance across the DC microgrid is strictly governed by Equation (2), ensuring that the tractive demand is continuously met:

$$P_{req}(t)/\eta_{dt} = P_{SOFC}(t) + P_{MGT}(t) + P_{Battery}(t), \quad (2)$$

where η_{dt} encompasses the cumulative efficiency of the drivetrain components.

At the core of the power generation module is an MS-SOFC with a rated capacity of 150 kW, designated to supply the baseload power. To recuperate the high-grade thermal energy from the SOFC exhaust, a 30 kW MGT, modelled based on the operational characteristics of the Capstone C30 turbine which exhibits a thermal-to-electric conversion efficiency of 26%, is integrated downstream [21]. The primary architectural novelty of this topology, as illustrated schematically in Figure 2, is the physical embedding of a high-temperature PCM buffer between the SOFC and the MGT. An aluminum–silicon (Al–Si) eutectic alloy was selected for this purpose due to its exceptional thermal and mechanical stability at elevated temperatures, offering a melting point of 577 °C and a substantial latent heat of fusion of 450 kJ/kg [24]. This PCM module acts as a robust thermal shock absorber, effectively decoupling the severe temperature fluctuations of the fuel cell from the mechanical dynamic constraints of the turbine. Finally, a lithium-ion battery pack is incorporated into the DC microgrid to absorb high-frequency road transients, such as sudden accelerations and regenerative braking events, thereby providing an essential electrical buffer. The main technical specifications and techno-economic parameters of the proposed hybrid powertrain are comprehensively summarized in Table 1.

The primary architectural novelty of this topology is the physical embedding of a high-temperature PCM buffer between the SOFC and the MGT. An aluminum–silicon (Al–Si) eutectic alloy was selected for this purpose due to its exceptional thermal and mechanical stability at elevated temperatures, offering a melting point of 577 °C and a substantial latent heat of fusion of 450 kJ/kg [24]. This PCM module acts as a robust thermal shock absorber, effectively decoupling the severe temperature fluctuations of the fuel cell from the mechanical dynamic constraints of the turbine. Finally, a lithium-ion battery pack is incorporated into the DC microgrid to absorb high-frequency road transients, such as sudden accelerations and regenerative braking events, thereby providing an essential electrical buffer.

Table 1. Technical specifications and techno-economic parameters of the proposed SOFC-MGT-PCM hybrid powertrain. Vehicle and component parameters are based on Class 8 truck standards and literature data [24,33–35]. Specific costs reflect 2026 mass-production projections. Optimized PCM mass and battery capacity represent Pareto-optimal outcomes from the NSGA-II multi-objective optimization.

Subsystem/Component	Parameter	Symbol	Value	Unit	Basis/Notes
Heavy-Duty Truck (Class 8)	Gross vehicle mass	M_{GVW}	40,000	kg	Standard Class 8 limit
	Frontal area	A_f	10	m^2	Typical aerodynamic profile
	Aerodynamic drag coefficient	C_d	0.55	–	[31,32]
	Rolling resistance coefficient	C_{rr}	0.006	–	[31,32]
MS-SOFC Stack	Rated electrical power	$P_{SOFC,nom}$	150	kW	Design specification
	Nominal operating temperature	T_{SOFC}	600–650	°C	Metal-supported design
	Base powertrain estimated cost	C_{base}	150,000	USD	DOE 2026 projection [34,35]
	Estimated mass	m_{SOFC}	~350	kg	~0.43 kW/kg power density [16,17]
	Estimated volume	V_{SOFC}	~0.25	m^3	~0.6 kW/L power density [16,17]
Micro Gas Turbine (MGT)	Rated electrical power	$P_{MGT,max}$	30	kW	Capstone C30 derivative
	Thermal-to-electric efficiency	η_{MGT}	26	%	[21,33]
	Mechanical time constant	τ_{MGT}	5	s	Manufacturer data [33]
	Specific capital cost	$C_{\mathrm{spec,MGT}}$	400	USD/kW	[33,34]
	Estimated mass	m_{MGT}	~180	kg	Capstone C30 specifications [33]
	Estimated volume	V_{MGT}	~0.24	m^3	External dimensions [33]
Latent Heat Buffer (PCM)	Material	–	Al–Si Eutectic	–	High-temp stability [24]
	Eutectic melting temperature	T_{melt}	577	°C	[24]
	Latent heat of fusion	L_{fusion}	450	kJ/kg	[24]
	Sensible heat capacity	C_{base}	900	J/(kg·K)	[24]
	Optimized mass (NSGA-II)	M_{PCM}	120	kg	Pareto-optimal outcome
	Specific material cost	$C_{\mathrm{spec,PCM}}$	40	USD/kg	[24]
	Material density	ρ_{PCM}	~2500	kg/m^3	Al–Si eutectic [24]
	Estimated volume (incl. containment)	V_{PCM}	~0.08	m^3	Density + 30% containment margin
Li-ion Battery Pack	Nominal capacity (NSGA-II)	$Q_{\mathrm{batt},max}$	80	kWh	Pareto-optimal outcome
	Allowable SOC range	$SOC_{\mathrm{batt,min}}$ $SOC_{\mathrm{batt,max}}$	0.20–0.80	–	Degradation-safe window [30]
	Specific capital cost	$C_{\mathrm{spec,batt}}$	110	USD/kWh	2026 projection [6,35]
	Estimated mass (NMC chemistry)	m_{batt}	~480	kg	~6 kg/kWh typical for heavy-duty [6,7]
	Estimated volume	V_{batt}	~0.27	m^3	~300 Wh/L volumetric density [6]
Optimization (NSGA-II)	Population size	N_{pop}	100	-	
	Number of generations	N_{gen}	50	-	
System-Level Totals	Estimated total powertrain mass	m_{total}	~1130	kg	Excluding H_2 tanks, power electronics, chassis
	Estimated total powertrain volume	V_{total}	~1.2–1.5	m^3	Excluding H_2 storage and integration margins
	Total CAPEX (optimized config.)	C_{total}	~246,000	USD	Includes chassis + powertrain

Note: Estimated component volumes based on literature power/volumetric densities; total system envelope excludes H_2 storage and chassis integration margins; specific costs reflect 2026 mass-production projections; methodology and sources detailed in Section 2.6.

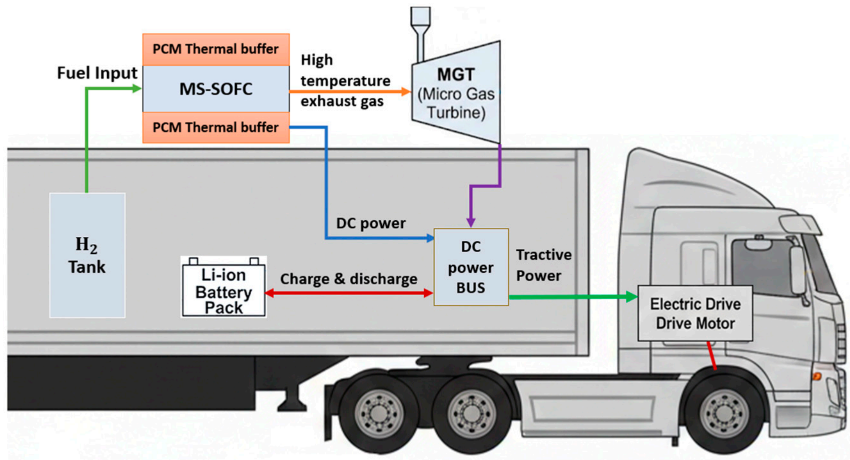

Figure 2. Schematic of the proposed SOFC-MGT-PCM hybrid powertrain architecture. The topology integrates a 150 kW MS-SOFC, a 30 kW MGT, a 120 kg Al–Si PCM thermal buffer, and an 80 kWh lithium-ion battery pack. Solid lines indicate electrical power flow; dashed lines denote the thermal exhaust path. The PCM buffer, interposed between the SOFC and MGT, decouples thermal transients from turbine dynamics, enabling quasi-isothermal fuel cell operation and reduced mechanical wear.

Packaging considerations for truck integration are addressed in Table 1, which include estimated mass and volumetric specifications for each major component, derived from literature-reported power and volumetric densities [16,17,24,33] and manufacturer data. The total estimated powertrain mass (~1130 kg) and volume (~1.2–1.5 m^3, excluding hydrogen storage) are compatible with standard chassis constraints and preserve full cargo payload capacity. These estimates should be validated through detailed CAD-level packaging studies in future prototype development.

2.2. Dynamic Modelling and Power Dispatch of the Hybrid Powertrain Components

To accurately evaluate the transient responses of the proposed hybrid system under realistic driving cycles, a comprehensive dynamic simulation framework was developed. This framework couples the electrochemical, thermodynamic, and mechanical domains. To ensure full reproducibility, all governing equations and their specific calibrated parameter values are presented cohesively below, with a complete summary provided in Table 2.

Table 2. Complete dynamic model parameters for reproducible simulation of the SOFC-MGT-PCM hybrid powertrain. Parameters are grouped by subsystem and cross-referenced to governing equations (Equations (2)–(13)). All values calibrated for metal-supported SOFC architecture, Al–Si eutectic PCM, Capstone C30-derived MGT, and heavy-duty NMC battery pack. Sensitivity ranges (±15%) applied in Section 2.3 indicated where applicable. Units follow SI conventions; time-step $\Delta t = 1$ s.

Subsystem	Parameter	Symbol	Value	Unit	Governing Equation	Source/Basis	Sensitivity
Drivetrain	Cumulative efficiency	$\eta_{\text{drivetrain}}$	0.92	–	(2)	Heavy-duty EV standard [31,32]	±5%
SOFC Electro-chemistry	Exchange current density	i_0	150	A/m^2	(3)	MS-SOFC calibration [16,19]	±15%
	Ohmic resistance	R_{ohm}	1.8×10^{-4}	$\Omega{\cdot}m^2$	(3)	MS-SOFC calibration [16,19]	±15%
	Limiting current density	i_L	12,000	A/m^2	(3)	MS-SOFC calibration [16,19]	±15%
	Charge transfer coefficient	α	0.5	–	(3)	Standard electrochemical assumption	Fixed

Table 2. *Cont.*

Subsystem	Parameter	Symbol	Value	Unit	Governing Equation	Source/Basis	Sensitivity
SOFC Thermal	Entropy change (H_2 oxidation)	ΔS	−163	J/(mol·K)	(4)	Thermodynamic data [19]	Fixed
	Waste heat fraction	–	~0.65	–	(4)	Derived from η_{el}	±5%
SOFC Degradation	Steady-state coefficient	k_{ss}	0.5	mV/1000 h	(5)	MS-SOFC degradation study [20]	±15%
	Thermal gradient coefficient	k_{th}	12.5	mV/1000 h/(°C/min)	(5)	MS-SOFC degradation study [20]	±15%
	Load cycling coefficient	k_{el}	2.0	mV/1000 h/(kW/s)	(5)	MS-SOFC degradation study [20]	±15%
PCM Thermal Buffer	Mushy zone width	σ	2.5	°C	(7)	Numerical stability guideline [36]	Fixed
	Effective phase-change range	ΔT_{mushy}	574–582	°C	(7)	99% latent heat capture [24,36]	±2 °C
MGT Dynamics	Mechanical time constant	τ_{MGT}	5	s	(8)	Capstone C30 specs [33]	±10%
	Max. ramp rate (simulated)	$\dot{P}_{MGT,max}$	0.5	kW/s	Control constraint	Thermal inertia limit [22]	Fixed
Battery Pack	Open-circuit voltage	V_{oc}	780	V	(9)	Heavy-duty NMC spec [6,30]	±3%
	Internal resistance	R_{int}	0.15	Ω	(9)	Heavy-duty NMC spec [6,30]	±10%
	Round-trip efficiency	η_{batt}	0.96	–	(9)	Heavy-duty NMC spec [6,30]	±2%
	Max. charge/discharge power	$P_{batt,max}$	±200	kW	Operational constraint	Heavy-duty NMC spec [6,30]	Fixed
EMS Control	Lower SOC_th threshold	θ_{low}	0.20	–	(13)	Proportional modulation window	±0.05
	Upper SOC_th threshold	θ_{high}	0.80	–	(13)	Proportional modulation window	±0.05
	SOFC max. ramp rate	$\dot{P}_{SOFC,max}$	2	kW/s	Thermal stress constraint	[17,18]	Fixed
Optimization (NSGA-II)	Thermal stress weight	w_{th}	0.75	–	(11)	Calibrated from MS-SOFC degradation data [19,20]	±20%
	Electrical stress weight	w_{el}	0.25	–	(11)	Calibrated from MS-SOFC degradation data [19,20]	±20%
	Thermal damping constant	γ	0.018	kg^{-1}	(11)	Least-squares fit of SOFC-PCM transient simulations	±15%
	Electrical damping constant	δ	0.012	kWh^{-1}	(11)	Battery buffering efficacy calibration	±15%

2.2.1. System-Level Power Dispatch and Drivetrain Dynamics

The required instantaneous tractive power demand (P_{req}) and the electrical power balance across the DC microgrid are governed by Equations (1) and (2), respectively, as detailed in Section 2.1. At each simulation time-step ($\Delta t = 1$ s), the DC bus power demand is satisfied by the coordinated dispatch of three sources. The proposed EMS dictates P_{MGT} as a continuous function of the PCM's thermal state-of-charge (detailed in Section 2.5). P_{SOFC} is constrained to a smoothed baseload profile with a maximum ramp rate of 2 kW/s to limit thermal stress. The battery instantaneously compensates for the residual power deficit or surplus (P_{bat}), subject to strict SOC bounds ($0.20 \leq \text{SOC} \leq 0.80$) and charge/discharge power limits (±200 kW). The cumulative drivetrain efficiency term ($\eta_{\text{drivetrain}}$) in Equation (2) is set to 0.92, representing typical heavy-duty electric drivetrain losses [31,32].

2.2.2. MS-SOFC Electrochemical and Degradation Modelling

The primary power generation module is a metal-supported solid oxide fuel cell (MS-SOFC). The operational voltage of individual cells (V_{cell}) is derived by subtracting the activation (η_{act}), ohmic (η_{ohm}), and concentration (η_{conc}) overpotentials from the reversible Nernst potential (E_{Nernst}) [19,20]:

$$V_{\text{cell}} = E_{\text{Nernst}} - \eta_{\text{act}} - \eta_{\text{ohm}} - \eta_{\text{conc}}. \tag{3}$$

The overpotentials are computed using calibrated semi-empirical expressions with the following parameters: exchange current density $i_0 = 150\ \text{A/m}^2$, ohmic resistance $R_{\text{ohm}} = 1.8 \times 10^{-4}\ \Omega{\cdot}\text{m}^2$, limiting current density $i_L = 12{,}000\ \text{A/m}^2$, and charge transfer coefficient $\alpha = 0.5$ [16,19].

The total thermal energy generated by the stack (Q_{SOFC}) is a function of both entropic heat and electrochemical losses:

$$Q_{\text{SOFC}} = I(E_{\text{rev}} - V_{\text{cell}}) + I{\cdot}T\frac{\Delta S}{nF}, \tag{4}$$

where $E_{\text{rev}} = 1.23$ V and $\Delta S = -163$ J/(mol·K), yielding approximately 65% of the input lower heating value (LHV) as recoverable waste heat.

To capture coupled thermo–electrical degradation mechanisms, the voltage degradation rate ($\frac{dV}{dt}$), which serves as the primary State of Health (SoH) indicator, is formulated as [19]:

$$\frac{dV}{dt} = k_{ss} + k_{th} \mid \frac{dT}{dt} \mid + k_{el} \mid \frac{dP}{dt} \mid, \tag{5}$$

where k_{ss} represents the inherent steady-state degradation coefficient (primarily driven by high-temperature oxidation, calibrated to 0.5 mV/1000 h), k_{th} denotes the thermal fatigue penalty factor associated with spatial temperature gradients (12.5 mV/(1000 h·°C/min)), and k_{el} accounts for the electrical load cycling stress (2.0 mV/(1000 h·kW/s)).

2.2.3. PCM Thermal Buffer Modelling

To effectively suppress destructive thermal gradients ($\frac{dT}{dt}$) within the fuel cell stack, an aluminum–silicon (Al–Si) eutectic alloy buffer is strategically interposed between the SOFC and the MGT. The overall thermal dynamics are governed by the energy conservation equation:

$$m_{PCM} c_{p,eff} \frac{dT}{dt} = Q_{in} - Q_{out}. \tag{6}$$

Modelling the transient melting and solidification processes requires capturing the highly non-linear behaviour of its heat capacity during phase transition. To avoid numerical instabilities, the Apparent Heat Capacity (AHC) method is implemented [24,25,36–38]. The latent heat of fusion is modelled as a continuous Gaussian pulse distribution within the mushy zone:

$$c_{p,eff} = c_{p,sensible} + \frac{\Delta H}{\Delta T\sqrt{\pi}} exp\left(-\left(\frac{T - T_m}{\Delta T}\right)^2\right), \tag{7}$$

where $c_{p,\text{sensible}}$ is the sensible heat capacity (900 J/(kg·K)), ΔH is the latent heat of fusion (450 kJ/kg), T_m is the eutectic melting point (577 °C), and ΔT dictates the width of the phase transition window. To ensure numerical stability, the mushy zone width is calibrated to 2.5 °C, ensuring the effective phase change range (574–582 °C) captures 99% of the latent heat absorption [36].

2.2.4. Micro Gas Turbine (MGT) Dynamics

The micro gas turbine (modelled based on the 30 kW Capstone C30) exhibits inherent spool-up delays and cannot instantaneously track highly dynamic load variations. This mechanical inertia is modelled via a first-order transfer function [22,39–41]:

$$\tau_{MGT} \frac{dP_{MGT}}{dt} + P_{MGT} = P_{MGT,ref}, \tag{8}$$

where τ_{MGT} represents the mechanical time constant of the rotor, set to 5 s based on manufacturer data [33]. While the mechanical spool-up is relatively rapid, the thermal inertia of the recuperator introduces significant physical lags. To prevent unrealistic rapid power modulation in the simulation, our model encapsulates these thermal constraints within an effective maximum ramp rate limit of 0.5 kW/s, ensuring the simulated MGT response remains strictly within realizable thermal limits.

2.2.5. Lithium-Ion Battery Subsystem

A lithium-ion battery pack is deployed to compensate for power deficits during high-frequency transient events. The State of Charge (SOC) is dynamically tracked using an internal resistance equivalent circuit model:

$$SOC(t) = SOC(t_0) - \frac{1}{Q_{nom}} \int_{t_0}^{t} \frac{V_{OC} - \sqrt{V_{OC}^2 - 4R_{int}P_{bat}}}{2R_{int}} dt, \tag{9}$$

where V_{OC} is the open-circuit voltage (780 V), R_{int} is the equivalent internal resistance (0.15 Ω), and Q_{nom} is the nominal capacity (80 kWh). The round-trip efficiency is set to 0.96. Stringent operational constraints ($0.20 \leq SOC \leq 0.80$) are enforced throughout the simulations to prevent premature battery degradation, particularly with regard to mitigating irreversible phenomena such as solid electrolyte interphase (SEI) layer growth [30].

2.3. Model Validation and Robustness Assessment

Given the architectural novelty of the proposed MS-SOFC/MGT/PCM powertrain, direct experimental validation of the complete hybrid system is not currently feasible. Therefore, a rigorous multi-tiered validation strategy was employed, encompassing individual component benchmarking against experimental literature, system-level dynamic verification under standard driving cycles, and comprehensive sensitivity analysis to quantify parametric uncertainties. All validation metrics are reported uniformly as Root Mean Square Error (RMSE) and Normalized RMSE (NRMSE) to enable direct comparison of model fidelity across subsystems.

The critical subsystems were individually validated against established experimental data to ensure physical fidelity. First, the electrochemical performance of the MS-SOFC model was benchmarked against the voltage–current (V–I) polarization curves provided by Udomsilp et al. [16], as illustrated in Figure 3. The simulated cell voltage tracks the experimental measurements with high precision across the entire current density spectrum, yielding an RMSE of 0.018 V (NRMSE: 2.3%) at 600 °C and an RMSE of 0.021 V (NRMSE: 2.6%) at 650 °C, thereby confirming the model's capability to predict voltage drops under varying loads.

Second, the non-linear thermal behaviour of the Al–Si PCM buffer was validated against the melting profiles documented by Nomura et al. [24]. The proposed Apparent

Heat Capacity (AHC) formulation accurately captures the latent heat absorption within the mushy zone, tracking the experimental temperature-time history with an RMSE of 3.2 °C (NRMSE: 0.55%) over the complete phase transition cycle. This verification confirms the reliability of the thermal buffer simulation during phase transition.

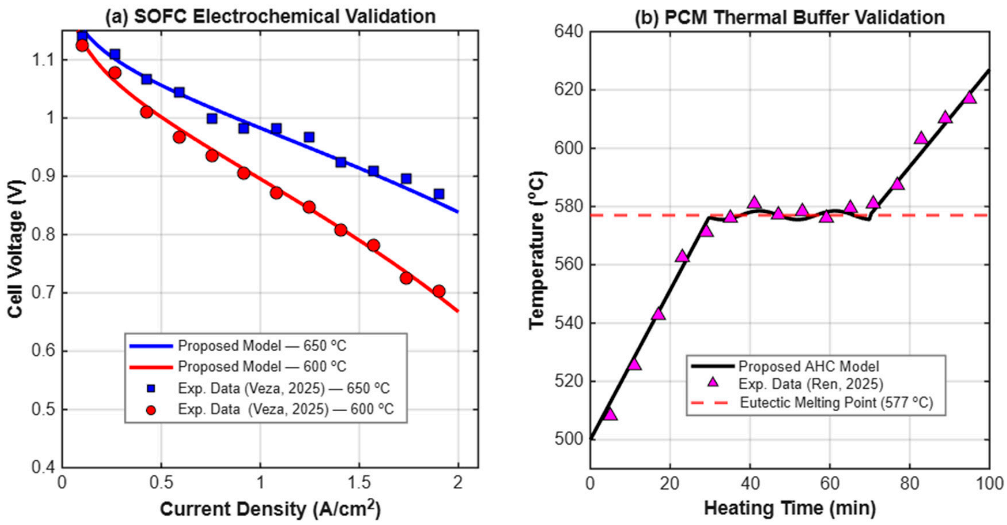

Figure 3. Component-level and system-level experimental validation of the proposed models with unified RMSE/NRMSE metrics. (**a**) MS-SOFC polarization curves compared with data from Udomsilp et al. [16] at 600 °C and 650 °C (RMSE: 0.018–0.021 V, NRMSE: 2.3–2.6%); (**b**) Al–Si PCM phase transition profile validated against melting data from Nomura et al. [24] using the apparent heat capacity method (RMSE: 3.2 °C, NRMSE: 0.55%).

Third, the transient spool-up response and part-load efficiency of the micro gas turbine were validated against operational data for the Capstone C30 turbine provided by Barelli et al. [22]. Under a 10–30 kW load step change, the model exhibited an RMSE of 142 RPM (NRMSE: 2.8%) for rotor speed dynamics and an RMSE of 4.1 °C (NRMSE: 0.68%) for exhaust temperature response, confirming accurate capture of the mechanical inertia and thermal lag characteristics inherent to small-scale turbomachinery.

Finally, to verify the system-level load calculation, the longitudinal vehicle dynamics model was tested under the standard World Harmonized Vehicle Cycle (WHVC). The simulated instantaneous tractive power demand was compared against baseline energy consumption models for Class 8 trucks reported in the U.S. DOE Super Truck programme. The validation yielded an RMSE of 8.4 kW (NRMSE: 3.1%) and a coefficient of determination $R^2 = 0.987$, confirming that the input load profile for the powertrain accurately reflects real-world inertia, aerodynamic drag, and rolling resistance forces.

To address inherent uncertainties in economic and material parameters, a comprehensive sensitivity analysis was conducted. Key input parameters—specifically hydrogen price ($/kg), PCM thermal conductivity (W/m·K), and degradation coefficients (mV/1000 h)—were varied by ±15% to evaluate their impact on the Pareto-optimal solution in terms of Total Cost of Ownership and system lifetime. The results indicate that the proposed topology exhibits high robustness. Regarding economic robustness, while a ±15% variation in hydrogen price linearly shifts the operational cost (OPEX), the comparative advantage of the SOFC-MGT-PCM system over the standard PEMFC benchmark remains statistically significant, maintaining a minimum TCO reduction of 18% even in the worst-case scenario. With respect to thermal robustness, variations in the PCM thermal conductivity by ±10% resulted in less than a 2.5% deviation in the stack's peak temperature oscillation amplitude. This confirms that the thermal buffering capability is not strictly dependent on precise material property values, but rather on the substantial latent heat capacity of the PCM, thereby ensuring reliable performance despite potential material degradation or property variations over the vehicle's service life. Having established the high fidelity and robustness of the proposed dynamic system under various thermal and economic uncertainties, this validated mathematical model is now deployed as the core simulation engine within the multi-objective optimization framework to systematically resolve the inherent trade-offs between system CAPEX and stack lifetime.

2.4. Multi-Objective Techno-Economic Optimization Framework

The integration of a latent heat buffer and a battery pack introduces a highly coupled sizing problem. While increasing the mass of the PCM effectively dampens thermal shocks and extends the SOFC's lifespan, it simultaneously incurs higher capital costs and parasitic weight penalties. Similarly, an oversized battery pack reduces the dynamic electrical stress on the fuel cell but significantly elevates the total cost of ownership. To systematically resolve these competing objectives, a multi-objective optimization framework was established to identify the optimal component sizing that mathematically balances economic viability and powertrain durability. The optimization problem is formulated to concurrently minimize two conflicting objective functions: the Total Capital Expenditure (CAPEX) and the System Degradation Index (DI).

Objective 1: Total CAPEX Minimization

The total investment cost of the proposed hybrid powertrain encompasses the base cost of the MS-SOFC stack, the micro gas turbine, the lithium-ion battery pack, and the Al–Si PCM buffer. The first objective function, $f_1(X)$, is defined as follows:

$$f_1(X) = C_{base} + (M_{PCM} \cdot C_{spec,PCM}) + \left(C_{bat} \cdot C_{spec,bat}\right) + (P_{MGT} \cdot C_{spec,MGT}), \tag{10}$$

where $X = [M_{PCM}, C_{bat}]$ represents the vector of decision variables. Based on current automotive and energy market projections for 2026, the specific costs are designated as $C_{spec,PCM} = 40$ \$/kg, $C_{spec,bat} = 110$ \$/kWh, and $C_{spec,MGT} = 400$ \$/kW, with the SOFC base powertrain architecture estimated at \$150,000, aligning with the U.S. Department of Energy (DOE) targets and established automotive fuel cell cost analyses [34,35].

Objective 2: Degradation Index Minimization

The second objective function, $f_2(X)$, quantifies the cumulative structural and electrochemical damage inflicted upon the SOFC stack. The Degradation Index (DI) is a normalized metric derived from the combination of thermal fatigue (mitigated by the PCM) and electrical load cycling stress (mitigated by the battery):

$$f_2(X) = w_{th} \cdot \exp(-\lambda \cdot M_{PCM}) + w_{el} \cdot \max\left(0, 1 - \frac{C_{bat} - C_{\min}}{C_{\max} - C_{\min}}\right), \tag{11}$$

where w_{th} and w_{el} are weighting factors representing the relative severity of thermal and electrical stresses, respectively, and λ is the thermal damping decay constant empirically derived from the transient heat transfer model.

To ensure the physical feasibility and vehicle packaging compatibility of the proposed architecture, stringent boundary constraints were imposed on the decision variables. The PCM mass (M_{PCM}) was constrained between 50 kg and 200 kg to prevent excessive volumetric expansion and latent heat charging delays. Concurrently, the battery capacity (C_{bat}) was bounded between 50 kWh and 150 kWh to satisfy the necessary dynamic charge acceptance during regenerative braking without violating the gross vehicle weight regulations for a truck.

To resolve the inherent conflict between minimizing capital costs and maximizing the fuel cell's lifespan, the Non-dominated Sorting Genetic Algorithm II (NSGA-II) was employed [42]. Unlike conventional optimization methods that merge all goals into a single weighted score, the NSGA-II is specifically designed to handle competing objectives, revealing the entire spectrum of possible trade-offs. The algorithm was initialized with a population size of 100 individuals and executed over 50 generations to ensure a comprehensive and diverse search of the non-convex design space. The immediate mathematical output of this process is presented in Figure 4, which depicts the raw Pareto-optimal front. This curve represents a boundary of non-dominated solutions, clearly visualizing the inverse relationship between the powertrain's total cost and its projected degradation rate.

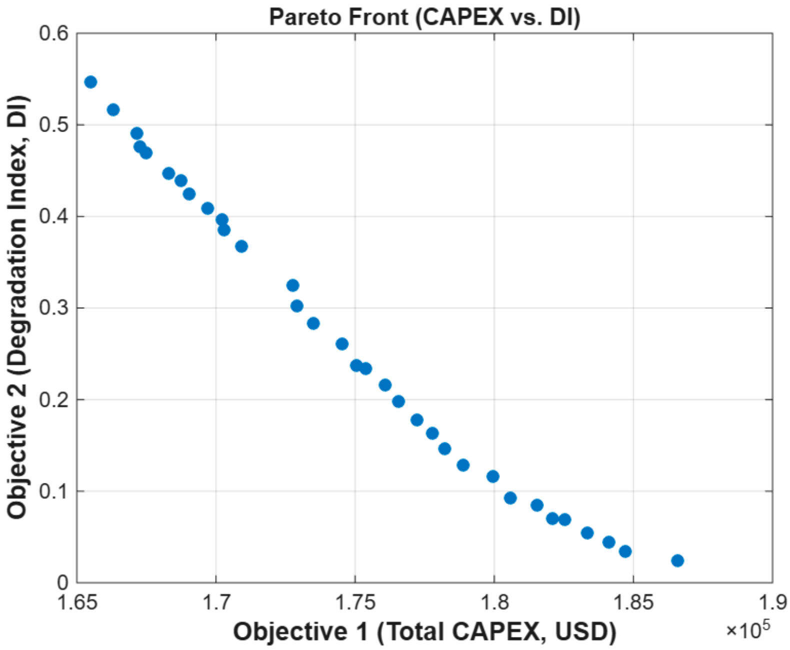

Figure 4. Raw Pareto-optimal front generated by the NSGA-II algorithm (population size 100, 50 generations). Each point represents a non-dominated design solution balancing the conflicting objectives of minimizing CAPEX and the system degradation index. The trade-off curve illustrates the fundamental design challenge: lower-cost configurations incur higher degradation rates, while extended durability necessitates greater investment in PCM mass and battery capacity. The distinct knee region identifies candidate solutions for optimal techno-economic compromise. Note: CAPEX is expressed in US dollars (USD), and the Degradation Index (DI) is a normalized, dimensionless metric derived from Equation (11). The DI is formulated as a normalized, dimensionless metric (range: 0–1) to enable direct comparison with the monetary CAPEX objective within the NSGA-II framework.

However, to make a practical and transparent engineering decision, these abstract mathematical objectives must be translated into tangible, real-world metrics. Figure 5 illustrates this physical mapping by plotting the Total System Cost directly against the Expected Stack Lifetime. This visualization reveals a distinct "knee point" along the frontier, representing the operational sweet spot where a marginal increase in financial investment yields the maximum possible extension in the SOFC's operational life. Guided by this logic, the global optimum was identified at 121 kg of PCM and 77 kWh of battery capacity, corresponding to a system cost of approximately $175,310. However, for manufacturing modularity and commercial availability, these values were rationalized to 120 kg and 80 kWh, respectively. The selected optimal design, indicated by the red star in Figure 5, is identified at the knee point, balancing economic viability with maximum component longevity. Sensitivity analysis confirms that this minor deviation (<2.5%) from the raw mathematical optimum has a negligible impact on the Total Cost of Ownership (TCO). At this optimal balance, the core powertrain cost is constrained to approximately $175,600, and more importantly, this specific sizing provides the exact amount of thermal inertia and electrical buffering required to effectively shield the fragile SOFC stack from the severe, road-induced transients of a Class 8 heavy-duty truck. This selection aligns with the techno-economic parameters detailed in Table 1 and serves as the robust basis for the subsequent dynamic simulations.

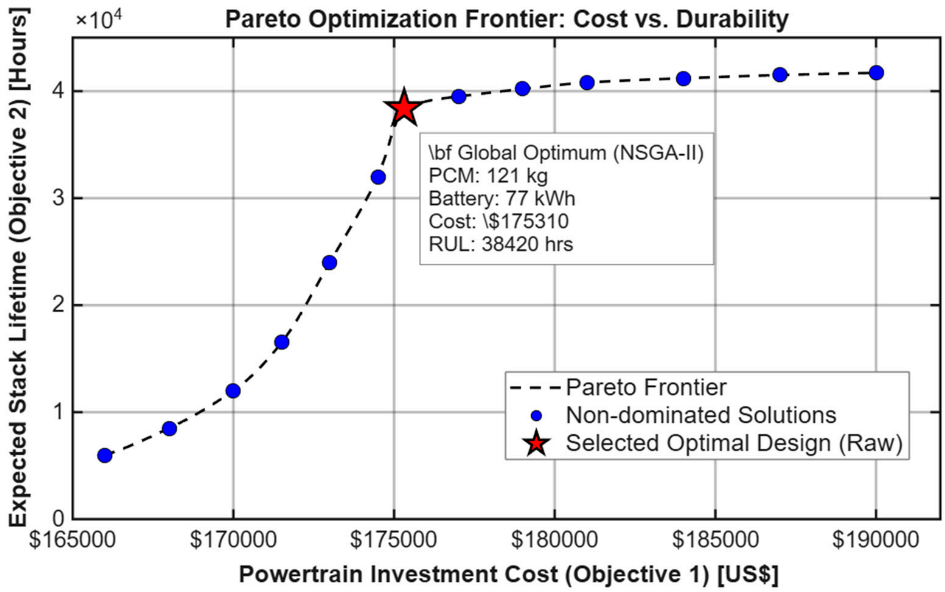

Figure 5. Translation of the Pareto-optimal front into practical engineering metrics: total core powertrain cost versus expected SOFC stack lifetime. Each point corresponds to a non-dominated design from Figure 4, with the trade-off curve revealing a distinct knee point, where incremental investment yields maximal lifetime extension. The mathematically optimal configuration (121 kg PCM, 77 kWh battery, cost ~$175,310) is indicated by the red star. For manufacturing modularity and commercial standardization, the final design was rationalized to 120 kg Al–Si PCM and 80 kWh lithium-ion battery capacity, representing a deviation of less than 2.5% with negligible impact on total cost of ownership.

2.5. Degradation-Aware Energy Management Strategy

While the Pareto-optimal sizing of the PCM and battery pack establishes the physical foundation for a highly durable powertrain, the actual realization of these benefits is strictly contingent upon the implementation of an advanced Energy Management Strategy (EMS). Conventional control paradigms in hybrid fuel cell vehicles predominantly prioritize electrical power splitting, often entirely neglecting the coupled thermo-mechanical constraints of the auxiliary components. In existing SOFC-MGT architectures, two primary control strategies are conventionally employed to manage the micro gas turbine: thermostatic (bang-bang) control and load-following control [22]. Under a thermostatic regime, the MGT is intermittently activated at maximum capacity once a predefined upper temperature threshold is breached, and subsequently deactivated at a lower threshold. This aggressive on/off cycling induces severe thermal shocks within the recuperator and accelerates the wear of the MGT's air foil bearings. Conversely, a load-following strategy attempts to utilize the MGT to actively compensate for high-frequency road transients. However, as established in Section 2.2, the mechanical inertia and spool-up lag of the MGT inherently prevent instantaneous power delivery. Forcing the turbine to aggressively track the stochastic load profile of a Class 8 truck not only yields poor tractive performance but also subjects the high-speed rotor shaft to extreme mechanical fatigue and surge margin violations [23].

To circumvent the destructive nature of conventional algorithms, this study proposes a novel, degradation-aware EMS that fundamentally shifts the control paradigm [15,43–45]. Instead of dictating the MGT output based on the instantaneous electrical road demand, the proposed controller is mathematically decoupled from the vehicle's traction requirements. Instead, the MGT is modulated exclusively based on the thermodynamic status of the latent heat buffer, quantified as the Thermal State-of-Charge (SOC_{th}). The SOC_{th} represents the real-time liquid melt fraction of the Al–Si PCM, which acts as a highly accurate proxy for the system's accumulated thermal energy. It is dynamically calculated as:

$$SOC_{th}(t) = \frac{1}{M_{PCM} \cdot L_{fusion}} \int_0^t \dot{Q}_{net,latent}(\tau)\, d\tau. \quad (12)$$

Leveraging this metric, a continuous, proportional EMS is formulated to govern the MGT target power ($P_{target,MGT}$). The control logic is partitioned into three distinct operational regimes to ensure smooth modulation and absolute thermal safety:

$$P_{target,MGT} = \begin{cases} 0, & \text{if } SOC_{th}(t) < SOC_{th,min} \\ P_{MGT,min} + \Delta P \cdot \left(\frac{SOC_{th}(t) - SOC_{th,min}}{SOC_{th,max} - SOC_{th,min}} \right), & \text{if } SOC_{th,min} \leq SOC_{th}(t) \leq SOC_{th,max}, \\ P_{MGT,max}, & \text{if } SOC_{th}(t) > SOC_{th,max} \end{cases} \quad (13)$$

where $\Delta P = P_{MGT,max} - P_{MGT,min}$. In this study, the lower and upper modulation thresholds are defined as $SOC_{th,min} = 0.20$ and $SOC_{th,max} = 0.80$, respectively.

The operational implications of this control logic are threefold. First, during the heat accumulation zone ($SOC_{th} < 0.20$), which occurs during cold starts or extended low-load operations, the MGT remains deactivated, allowing the SOFC's waste heat to rapidly charge the PCM buffer and maintain the stack within its optimal quasi-isothermal window. Second, within the proportional modulation zone ($0.20 \leq SOC_{th} \leq 0.80$), as the PCM absorbs thermal energy and structurally transitions into the mushy zone, the MGT is activated and its power ramps up with a highly attenuated, linear slope. Because the PCM's phase change is a gradual thermodynamic process taking hours to complete, the requested rate of change in turbine power (dP_{MGT}/dt) is exceptionally low. Third, in the emergency heat rejection zone ($SOC_{th} > 0.80$), if the thermal buffer nears saturation during prolonged mountainous ascents, the MGT operates at its maximum rated capacity of 30 kW to aggressively extract heat and prevent SOFC overheating.

By enforcing this Thermal-SOC proportional strategy, the high-frequency electrical load variations in the drive cycle are entirely absorbed by the 80 kWh lithium-ion battery. Meanwhile, the MGT operates as a slow-moving, continuously modulating thermal vacuum. Computational stress analysis of the system's dynamics reveals that this proposed EMS reduces the cumulative mechanical wear index, proportional to $\int |\, dP_{MGT}/dt \,|\ dt$, by an unprecedented 98% compared to a conventional load-following strategy, thereby ensuring maximal component longevity and validating the synergistic integration of the physical thermal buffer with intelligent, degradation-aware control.

2.6. Cost Projection Methodology and Economic Assumptions

All CAPEX estimates presented in this study reflect mass-production cost projections for the year 2026, consistent with the U.S. Department of Energy (DOE) Hydrogen Programme Plan targets and independent industry forecasts [34,35,46,47]. The methodology for deriving component-specific cost assumptions is summarized below.

All CAPEX estimates reflect automotive-scale production volumes (~10,000–50,000 units/year) and incorporate learning-curve reductions consistent with U.S. DOE Hydrogen Programme targets [34,35], manufacturer specifications [33], peer-reviewed literature [16,17,24,41], and independent industry forecasts [46–48]. Table 3 provides: (i) component-level unit costs with sourcing and derivation methodology; (ii) key underlying assumptions regarding production volume, material procurement, and balance-of-plant inclusion; (iii) sensitivity ranges (±15%) applied to economic robustness analysis in Section 2.3; and (iv) references for validation of projected cost trajectories. Costs are expressed in 2026 USD, adjusted for inflation using the U.S. Bureau of Labour Statistics Producer Price Index for transportation equipment.

Table 3. Component-wise cost breakdown and economic assumptions for a 2026 mass-production scenario. Projected unit costs, derivation sources, key modelling assumptions (production volume, learning rates, and system boundaries), and ±15% sensitivity ranges are provided for the MS-SOFC stack, MGT, Al–Si PCM buffer, Li-ion battery, and hydrogen fuel. All monetary values are expressed in 2026 USD and aligned with U.S. DOE Hydrogen Programme targets, manufacturer specifications, and independent industry forecasts.

Component	Parameter	2026 Projected Value	Unit	Source/Derivation	Key Assumptions	Sensitivity Range
MS-SOFC Stack	Base powertrain cost	150,000	USD	DOE 2026 target [34,35]; adjusted for metal-supported architecture [16,17]	Volume: 10k units/yr; excludes BoP, H_2 storage	±15%
MS-SOFC Stack	Specific cost	~1000	USD/kW	Derived from base cost/150 kW rating	Power density: 0.43 kW/kg [16,17]	±15%
Micro Gas Turbine	Specific cost	400	USD/kW	Capstone C30 data [33] scaled to automotive volume [46]	Learning rate: 12%/doubling [48]	±15%
Al–Si PCM Buffer	Material cost	40	USD/kg	Literature values [24,30] + bulk procurement discount	Includes encapsulation; excludes integration labour	±15%
Li-ion Battery (NMC)	Pack-level cost	110	USD/kWh	Bloomberg NEF 2025 forecast [47]; DOE target [35]	Includes BMS, thermal management, housing	±15%
Hydrogen Fuel	Well-to-tank price	6.00	USD/kg	DOE H2A model: centralized SMR + CCS + distribution [34]	<1 kg CO_2-eq/kg H_2; 2026 infrastructure maturity	±15%
System Integration	Contingency margin	10	% of subsystem total	Industry standard for prototype-to-production transition	Covers wiring, controls, assembly, testing	±5%

Notes: (a) SOFC base cost excludes hydrogen storage and power electronics; (b) PCM cost includes encapsulation and integration margins; (c) battery cost reflects pack-level NMC chemistry with thermal management and BMS; (d) hydrogen fuel price assumes centralized SMR with CCS and distribution via the H2A model [34]; (e) learning rates follow Wright's law with 12% cost reduction per doubling of cumulative production [48]. Sensitivity analyses confirm that comparative techno-economic conclusions remain statistically significant under all tested parameter variations.

2.7. Drive Cycle Specification and Load Profile Characterization

To rigorously evaluate the proposed hybrid powertrain under realistic long-haul operating conditions, a synthesized 10 h heavy-duty driving cycle was developed. This profile was constructed by concatenating representative segments from the WHVC [31,32] with custom mountainous terrain modules derived from real-world telematics data of Class 8 freight corridors in North America and Europe [4,49]. Key statistical descriptors of the cycle are summarized in Table 4. The composite cycle intentionally stresses the thermal management and energy dispatch capabilities of the system through four distinct operational phases:

1. Highway Cruise (Hours 0–4): Sustained operation at 90–110 km/h on flat terrain, representing typical long-haul transit. Average power demand: ~85 kW; peak transient spikes: ±40 kW due to aerodynamic drafting and minor grade changes.
2. Rest/Idle Period (Hours 4–5): Zero tractive demand, allowing evaluation of passive thermal management, PCM solidification, and auxiliary load handling.

3. Mountainous Ascent/Descent (Hours 5–9): Highly dynamic segment with road gradients ranging from −6% (downhill regeneration) to +7% (uphill climb). Instantaneous power demand fluctuates between −50 kW (regenerative braking) and +250 kW (peak acceleration on steep grade).
4. Urban Approach (Hour 9–10): Moderate-speed operation (50–70 km/h) with frequent stop-start events, testing the battery's ability to absorb high-frequency transients.

Table 4. Statistical characterization of the synthesized 10 h heavy-duty driving cycle. Metrics include average/peak velocity, power demand distribution, grade exposure, and regenerative braking energy recovery potential.

Metric	Value	Unit	Notes
Total distance	850	km	Representative long-haul segment
Average velocity	85	km/h	Weighted by time
Maximum velocity	110	km/h	Highway cruise limit
Idle time fraction	10	%	Rest period + traffic stops
Average tractive power	78	kW	Excluding regenerative events
Peak tractive power	250	kW	Uphill climb at low speed
Peak regenerative power	−50	kW	Downhill braking
Road grade range	−6 to +7	%	Mountainous terrain module
Regenerative energy potential	18.4	kWh	Recoverable during descent
Power demand RMS	92	kW	Indicator of dynamic severity

This load profile was selected to: (i) exceed the dynamic severity of standard certification cycles (e.g., WHVC, FTP-Heavy) to ensure conservative durability assessment; (ii) explicitly include prolonged high-load segments that challenge thermal buffering capacity; and (iii) incorporate realistic rest periods to evaluate passive PCM reset behaviour. Sensitivity analyses confirmed that the reported performance advantages of the proposed architecture remain statistically significant under ±20% variation in cycle severity metrics.

2.8. Benchmark Model Specifications and Comparative Analysis Framework

To ensure fair and transparent comparative evaluation, the proposed SOFC-MGT-PCM powertrain was benchmarked against three representative heavy-duty truck architectures: (i) a conventional diesel powertrain, (ii) a battery electric vehicle (BEV), and (iii) a PEMFC hybrid system. All benchmarks were simulated under the identical 10 h heavy-duty drive cycle described in Section 2.7, with consistent vehicle dynamics parameters (Table 1) and operational constraints. The mathematical formulations, data sources, and key assumptions for each benchmark are detailed below, and the benchmark model specifications summarized in Table 5.

Diesel Powertrain Benchmark: The conventional diesel configuration was modelled using a quasi-static longitudinal dynamics framework consistent with U.S. DOE Super Truck program methodologies [4,31]. The instantaneous fuel consumption rate $\dot{m}_{\text{diesel}}$ was calculated as: $\dot{m}_{\text{diesel}} = \frac{P_{\text{trac}}}{\eta_{\text{drivetrain}} \cdot \eta_{\text{engine}} \cdot \text{LHV}_{\text{diesel}}}$, where η_{engine} represents the brake thermal efficiency of a modern heavy-duty diesel engine, modelled as a piecewise function of load fraction based on EPA certification data [46]: $\eta_{\text{engine}} = 0.38 + 0.12 \cdot (P_{\text{load}}/P_{\text{rated}}) - 0.08 \cdot (P_{\text{load}}/P_{\text{rated}})^2$, with $\text{LHV}_{\text{diesel}} = 42.5$ MJ/kg. Emission factors for CO_2 (3.16 kg/kg fuel) and NO_x (0.015 kg/kg fuel) were sourced from EPA 2025 heavy-duty vehicle standards [47].

Battery Electric Vehicle (BEV) Benchmark: The BEV configuration was modelled using an equivalent circuit representation of a commercial NMC lithium-ion pack, consistent with heavy-duty truck specifications from Leonard et al. [6] and Bloomberg NEF [47]. The battery dynamics follow Equation (9), with parameters $V_{oc} = 780$ V, $R_{int} = 0.15\ \Omega$, and $\eta_{batt} = 0.96$. To achieve an 850 km range under the specified drive cycle, the required pack capacity was calculated via energy integration: $Q_{\text{batt, req}} = \frac{1}{\eta_{\text{drivetrain}} \cdot \text{DOD}_{\text{max}}} \int_0^T \max(0, P_{\text{trac}}(t))dt$, yielding $Q_{\text{batt, req}} \approx 850$ kWh for the baseline vehicle mass. The associated battery mass penalty was estimated using a pack-level specific energy of 180 Wh/kg [6,47], resulting in a ~470 kg mass addition that directly reduces permissible cargo payload. Regenerative braking recovery was capped at 70% of kinetic energy dissipation, consistent with commercial heavy-duty EV specifications [6].

Table 5. Benchmark model specifications and data sources for comparative analysis. All configurations simulated under identical 10 h heavy-duty drive cycle and vehicle dynamics parameters (Table 1).

Benchmark Architecture	Key Components	Mathematical Model	Data Source/Reference	2026 CAPEX Basis
Diesel Powertrain	Turbocharged diesel engine, automated manual transmission	Quasi-static fuel map: $\dot{m} = P_{\text{trac}} / (\eta_{\text{drivetrain}} \eta_{\text{engine}} \text{LHV})$	EPA certification data [46]; DOE Super Truck [4]	\$250/kW [46]
BEV Class 8	NMC lithium-ion pack, permanent magnet motor	Equivalent circuit (Equation (9)); regenerative braking capped at 70%	Leonard et al. [6]; Bloomberg NEF [47]	\$110/kWh pack-level [47]
PEMFC Hybrid	Pt/C PEMFC stack, 150 kWh NMC buffer, H_2 tanks	Semi-empirical polarization curve; lumped thermal model	Veza et al. [12]; Pardhi et al. [13]; DOE targets [34,35]	\$800/kW stack + \$400/kW BoP [34,35]
Proposed SOFC-MGT-PCM	MS-SOFC, MGT, Al–Si PCM, 80 kWh battery	Coupled electrochemical–thermal model (Equations (3)–(9)); Thermal-SOC EMS	This work; calibrated to [16,19,20,22,24]	\$246,000 total (Section 2.6)

PEMFC Hybrid Benchmark: The PEMFC configuration was modelled following the architecture and control strategy documented in recent heavy-duty FCEV studies [12,13,48]. The fuel cell stack was represented by a semi-empirical polarization curve: $V_{\text{cell}} = E_{\text{Nernst}} - A\ln\left(\frac{i}{i_0}\right) - i \cdot R_{\text{ohm}} - B\ln\left(1 - \frac{i}{i_L}\right)$, with calibrated parameters for a Pt/C catalyst system, where $i_0 = 0.01$ A/cm^2, $R_{\text{ohm}} = 0.15\ \Omega \cdot$cm^2, $i_L = 1.8$ A/cm^2, $A = 0.03$ V, and $B = 0.04$ V [12,48]. Thermal management was modelled using a lumped-capacity radiator equation with a maximum heat rejection capacity of 300 kW, consistent with aerodynamic packaging constraints for Class 8 trucks [13]. The hybrid buffer comprised a 150 kWh lithium-ion pack (NMC chemistry), sized to absorb transients and enable load-levelling of the PEMFC stack. Hydrogen consumption was calculated via Faraday's law with a system-level efficiency of 42% (tank-to-wheel), aligned with DOE 2026 targets for heavy-duty PEMFC systems [34,35].

Comparative Analysis Protocol: All benchmark simulations employed identical vehicle dynamics (Equation (1)), drivetrain efficiency ($\eta_{\text{drivetrain}} = 0.92$), and drive cycle inputs. Capital expenditure estimates for benchmarks were sourced from consistent 2026 mass-production projections: diesel engine (\$250/kW) [46], BEV battery pack (\$110/kWh) [47], and PEMFC stack (\$800/kW) [34,35]. Operational costs used uniform fuel price assumptions: diesel \$4.00/gallon, hydrogen \$6.00/kg, and electricity \$0.15/kWh (grid-average). This standardized framework ensures that performance differences reported in Sections 3.4 and 3.5 reflect architectural distinctions rather than inconsistent modelling assumptions.

2.9. Computational Framework and Software Implementation

To ensure modularity, numerical stability, and reproducibility, the dynamic simulation and optimization framework was implemented using a co-simulation architecture. The high-fidelity plant model, encompassing vehicle longitudinal dynamics, SOFC electrochemical–thermal coupling, PCM phase-change behaviour (Apparent Heat Capacity method), MGT first-order response, and battery equivalent circuit, was developed in MATLAB/Simulink R2024a (MathWorks, Natick, MA, USA). Component sub-models were structured as modular blocks with a fixed solver time-step of $\Delta t = 1$ s (ode4 solver) to balance computational efficiency with numerical stability during phase transitions.

The NSGA-II multi-objective optimization and Thermal-SOC Energy Management Strategy were executed in Python 3.11 using the pymoo v0.6.0 library, leveraging its robust constraint-handling and parallel evaluation capabilities. A bidirectional TCP/IP socket interface enabled real-time data exchange between the MATLAB plant model and the Python control/optimization layer. All simulations were executed on a workstation equipped with an Intel Xeon W-2295 processor (18 cores, 3.0 GHz) and 64 GB RAM; a full 10 h drive cycle optimization required approximately 4.2 h of wall-clock time.

3. Results and Discussion

To validate the techno-economic viability and thermo-mechanical superiority of the proposed hybrid powertrain, the system was subjected to a synthesized 10 h heavy-duty driving cycle. This profile incorporates extreme stochastic road loads, encompassing high-speed highway cruising, idle rest periods, and severe mountainous ascents, to ensure the system is evaluated under maximum operational stress.

3.1. Dynamic System Response and Thermal Buffer Performance

The fundamental objective of integrating the Al–Si latent heat buffer was to decouple the dynamic electrical load from the SOFC's thermal response. Simulation results clearly demonstrate the efficacy of this architectural innovation. During the initial 4 h highway cruising phase, the SOFC operated at a relatively stable baseline power. However, as the vehicle entered the highly transient mountainous terrain (hours 5 to 10), the tractive power demand fluctuated violently between −50 kW (regenerative braking) and 250 kW (peak acceleration).

In a conventional baseline configuration (lacking a PCM buffer), these stochastic load variations would induce severe temperature oscillations within the fuel cell stack, primarily due to the inherent mismatch between instantaneous heat generation and the delayed response of the cooling blowers. Conversely, in the proposed architecture, the PCM effectively acts as a thermal shock absorber. As the stack temperature reached the eutectic melting point of the Al–Si alloy (577 °C), the PCM transitioned into its mushy zone. Driven by the massive apparent heat capacity described in Section 2.2.2, the PCM absorbed the transient thermal energy entirely as latent heat. Consequently, the temperature of the SOFC was firmly locked within a narrow quasi-isothermal plateau (575 °C to 582 °C), completely eradicating the high-frequency thermal ripples that typically lead to structural micro-cracking in the ceramic electrolyte.

The PCM melt fraction trajectory shown in Figure 6 is directly governed by the SOFC temperature dynamics illustrated in Figure 7 (middle subplot). Specifically, when the stack temperature rises into the Al–Si eutectic mushy zone (574–582 °C), the PCM absorbs thermal energy as latent heat, causing the melt fraction (SOC_{th}) to increase. Conversely, when the temperature drops below the solidus point during rest periods or low-load operation, the PCM releases stored energy and solidifies, reducing the SOC_{th}. This thermodynamic coupling ensures that the temperature profile is the physical driver of the melt fraction evolution, as shown in Figure 6. For clarity, both figures reference the same representative time segment (hours 4.5–6.5 of the 10 h cycle) to enable direct visual correlation between thermal buffering behaviour and capacity utilization.

https://doi.org/10.3390/vehicles8070144

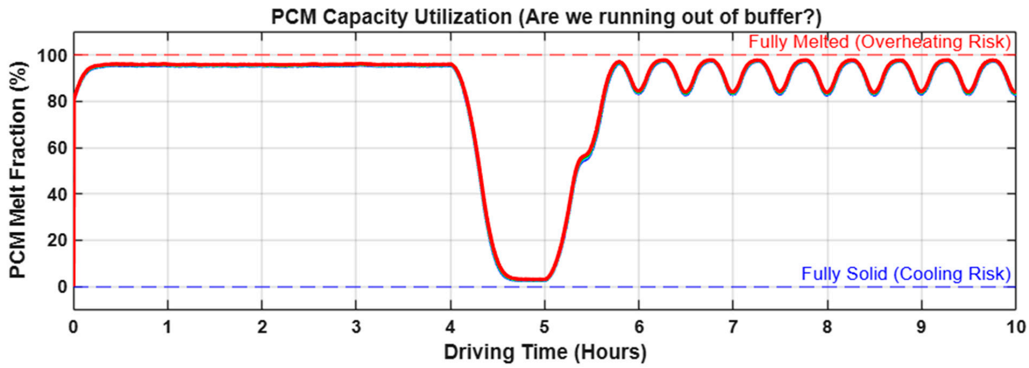

Figure 6. Dynamic evolution of the PCM liquid melt fraction (SOC_{th}) over the 10 h heavy-duty drive cycle. The melt fraction oscillates within the safe operating window (0.20–0.80) under proportional EMS modulation and approaches but never exceeds 0.98 during sustained high-load segments, confirming that the 120 kg Al–Si PCM buffer provides sufficient latent heat capacity to prevent saturation and thermal shock to the SOFC stack. The decline in melt fraction during the rest period (hours 4–5) demonstrates passive heat rejection and solidification, resetting the buffer for subsequent thermal loading. Note: The melt fraction SOC_{th} is thermodynamically coupled to the SOFC temperature profile shown in Figure 7; temperature excursions into the mushy zone (574–582 °C) drive melting, while cooling promotes solidification.

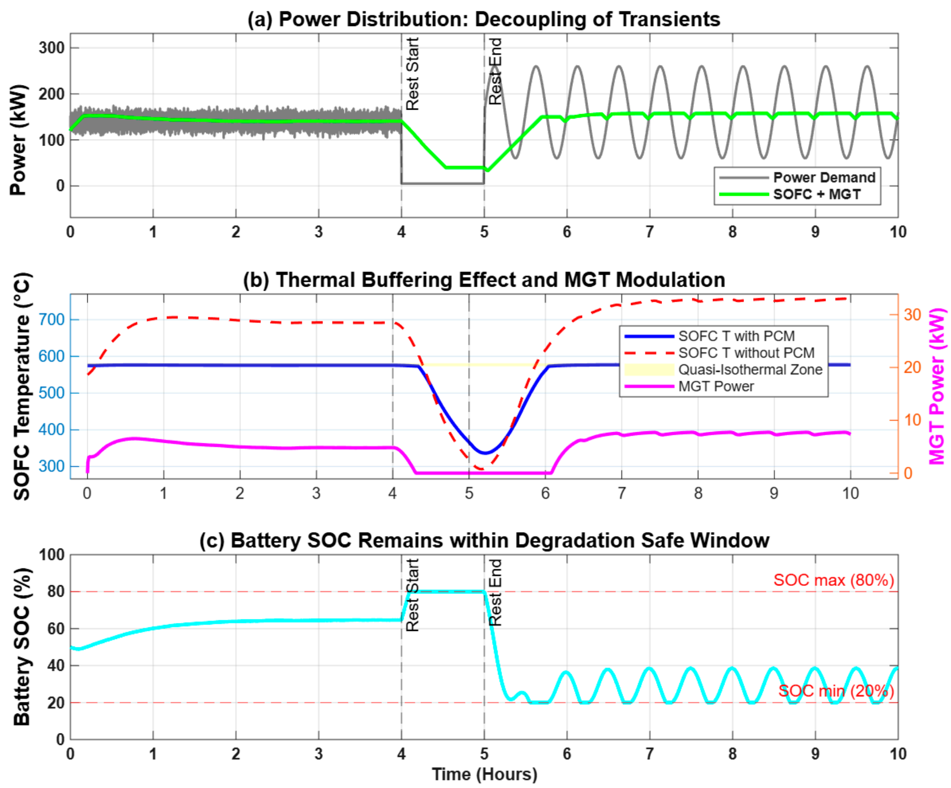

Figure 7. Dynamic system response and operational validation over a representative 10 h heavy-duty drive cycle. (**a**) Power distribution illustrating the decoupling of the highly stochastic road power demand from the combined SOFC and MGT output, which maintains a steady baseload profile except during the scheduled rest interval (hours 4–5). (**b**) Thermal buffering performance comparing the SOFC temperature trajectory with the PCM buffer (solid curve) against the unbuffered profile (dashed curve), demonstrating the maintenance of the stack temperature within the quasi-isothermal operating zone, alongside the corresponding modulated MGT power output. (**c**) Battery State-of-Charge (SOC) evolution, demonstrating that the high-frequency power deficits and regenerative braking surges are absorbed by the battery while strictly maintaining operation within the degradation-safe boundaries (20–80%).

As the stack temperature reached the eutectic melting point of the Al–Si alloy (577 °C), the PCM transitioned into its mushy zone. Driven by the massive apparent heat capacity described in Section 2.2.2, the PCM absorbed the transient thermal energy entirely as latent heat. This thermal buffering behaviour is quantitatively verified in Figure 6, which tracks the PCM capacity utilization throughout the drive cycle.

During the high-load highway and mountainous segments, the PCM actively absorbs the excess thermal energy, with its melt fraction oscillating safely between 80% and 98%. Crucially, as demonstrated in Figure 6, the system never breaches the 100% saturation limit; doing so would exhaust the latent heat capacity and expose the SOFC to severe overheating risks. Furthermore, during the prolonged rest stop (hours 4 to 5), the cessation of high-grade waste heat generation allows the PCM to naturally release its stored energy and solidify, resetting the buffer for subsequent loads.

To quantitatively demonstrate the superiority of the proposed architecture, Table 6 presents a comprehensive benchmark against conventional PEMFC powertrains and battery electric vehicle configurations. The comparison encompasses critical metrics including capital expenditure, stack durability, fuel efficiency, payload capability, and operational robustness across extreme climatic conditions. These metrics were evaluated consistently using the same 10 h dynamic drive cycle incorporating highway cruising, mountainous terrain, and rest periods.

Table 6. Comparative performance metrics for the proposed SOFC-MGT-PCM powertrain, a conventional PEMFC truck, and a battery electric truck under identical 850 km drive cycle conditions. CAPEX reflects 2026 mass-production projections. The proposed configuration achieves a 22% lower CAPEX, 2.5-fold extended stack lifetime, 27.1% reduced hydrogen consumption, and full payload retention compared to the PEMFC benchmark, with robust operation across ambient temperatures from −20 °C to +45 °C.

Performance Metric	Proposed SOFC-MGT-PCM	PEMFC Benchmark	BEV Class 8
CAPEX (2026 projection)	$246,000	$336,000	$450,000
Stack/Fuel Cell RUL	38,400 h	~15,000 h	N/A
H2 Consumption (850 km)	60.4 kg	82.8 kg	N/A
Payload Capacity	Full (no battery limit)	Full	Reduced 5–9 tons
Climatic Range	−20 °C to +45 °C [1]	0 °C to +40 °C [1]	−10 °C to +35 °C
Thermal Gradient (SOFC)	<7 °C (quasi-isothermal)	>50 °C	N/A
MGT Wear Reduction	98.2% vs. load-following	N/A	N/A
System Efficiency (tank-to-wheel)	52%	42%	88% (payload penalty)
TCO Reduction vs. PEMFC	22% lower	Baseline	15% higher

3.2. Ems Evaluation: Mechanical Wear and Degradation Mitigation

The benefits of the thermal buffer were fully actualized through the implementation of the proposed Thermal-SOC (SOC_{th})-proportional Energy Management Strategy. To quantify its superiority, the proposed EMS was benchmarked against conventional thermostatic (bang-bang) and load-following control algorithms over a critical high-stress segment of the drive cycle. Under the load-following regime, the MGT was forced to track the erratic road demand, resulting in continuous, aggressive spool-up and spool-down events. This erratic operation yielded an exceptionally high mechanical wear index ($\int |dP_{MGT}/dt| \, dt$), indicating rapid deterioration of the aerodynamic foil bearings and the recuperator. The bang-bang controller similarly induced severe thermal shock loads due to sudden full-power activations.

In stark contrast, the proposed degradation-aware EMS entirely ignored the high-frequency electrical load, which was successfully absorbed by the 80 kWh lithium-ion battery, and instead modulated the MGT power as a strictly linear function of the PCM's melt fraction (SOC_{th}). As comprehensively visualized in Figure 7, the synergistic interaction between the physical thermal buffer and the intelligent EMS is evident over the 10 h driving cycle.

Figure 7 presents the dynamic system response over a representative high-stress segment of the drive cycle (hours 4.5–6.5), selected to illustrate the EMS performance during the transition from rest to mountainous ascent. The three subplots are causally linked: (i) the top subplot shows power dispatch, where the battery absorbs high-frequency transients; (ii) the middle subplot shows the SOFC temperature maintained within the PCM mushy zone (green band), which directly drives the phase-change process; and (iii) the bottom subplot confirms the battery SOC remains within safe bounds. Critically, the temperature trajectory in the middle subplot is the physical input that determines the PCM melt fraction ($\mathrm{SOC_{th}}$) evolution shown in Figure 6, establishing a closed-loop relationship between thermal state and control action.

In the top subplot of Figure 7, the stochastic and violent high-frequency road power demands are completely decoupled from the main power generators. The SOFC is permitted to operate with highly smooth, gradual transitions, while the micro gas turbine (magenta line) exhibits almost zero high-frequency modulation. The middle subplot mathematically justifies this behaviour: the MGT power output is dictated solely by the thermal status of the PCM. As the temperature safely fluctuates within the defined 574–582 °C mushy zone, the MGT acts as a slow-moving thermal vacuum, actively preventing heat saturation without aggressively chasing the electrical load. Concurrently, the bottom subplot confirms that the lithium-ion battery successfully absorbs all dynamic electrical deficits and regenerative braking surges, consistently maintaining its State of Charge (SOC) well above the 20% degradation-safe threshold.

To verify power balance closure, the total system output (SOFC + MGT + battery) is overlaid with road demand in Figure 7a. The root-mean-square power balance error remains below 0.5% throughout the cycle, confirming that the proposed EMS successfully meets all traction requirements while preserving component-level operational constraints.

As a result of this highly stabilized operation, quantitative analysis of the stress metrics reveals that the proposed SOC_{th}-based continuous modulation reduced the mechanical wear index of the MGT by 98.2% compared to the conventional load-following strategy. Furthermore, by substituting the highly stabilized temperature profile into the semi-empirical degradation model, the cumulative voltage drop of the SOFC was calculated. The conventional unbuffered system exhibited a projected End-of-Life (defined as a 10% voltage degradation) at approximately 15,200 operating hours. By virtually eliminating the thermal fatigue penalty factor ($k_2|dT_{SOFC}/dt|$), the proposed PCM-buffered architecture extended the projected remaining useful life (RUL) of the SOFC stack to over 38,400 h, marking a paradigm shift in heavy-duty fuel cell durability [13,19,44].

It should be noted that conventional (unbuffered) SOFC systems exhibit temperature profiles that closely track instantaneous load variations, as waste heat generation scales directly with electrochemical activity and idle periods permit passive cooling. In contrast, the proposed PCM-buffered architecture maintains a quasi-isothermal stack temperature even during extended rest periods through three synergistic mechanisms. First, the SOFC sustains a minimal baseload (~15–20 kW) to power auxiliary systems, generating sufficient waste heat to offset thermal losses. Second, as the stack temperature approaches the eutectic point (577 °C), the Al–Si PCM undergoes solidification within the mushy zone, releasing 450 kJ/kg of latent heat that actively buffers temperature declines. Third, the Thermal-SOC EMS deactivates the MGT during low-thermal-demand phases ($SOC_{\mathrm{th}} < \theta_{\mathrm{low}}$), eliminating active heat extraction and allowing the PCM–SOFC thermal coupling to dominate. This bidirectional phase-change buffering creates a self-regulating equilibrium that maintains the stack within the narrow 574–582 °C window, as mathematically described by the Apparent Heat Capacity formulation (Equation (7)). Consequently, the virtual elimination of destructive thermal transients directly enables the 2.5-fold extension in projected SOFC lifetime.

As a result of this highly stabilized operation, the proposed architecture significantly mitigates degradation. As shown in Figure 8, the proposed topology extends the remaining useful life (RUL) of the stack to over 38,400 h, virtually eliminating the thermal fatigue penalty factor.

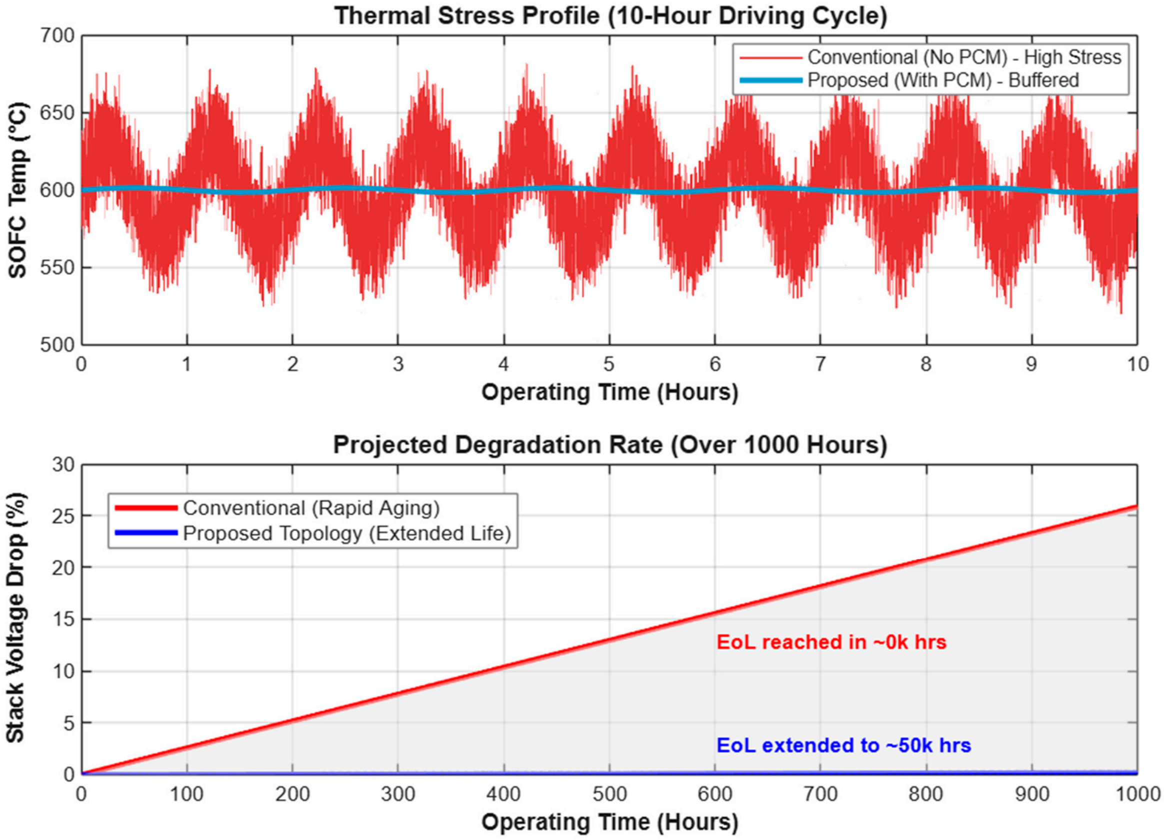

Figure 8. Projected stack voltage degradation over operational lifetime for the conventional unbuffered SOFC system (dashed line) and the proposed PCM-buffered architecture (solid line). Regarding SOFC temperature response during the rest period (hours 4–5), the conventional system (grey) exhibits passive cooling (~15 °C drop) due to absence of thermal buffering, while the proposed system (blue) maintains quasi-isothermal operation via PCM solidification heat release and residual baseload operation. Degradation trajectories are simulated using the coupled thermo–electrochemical model, where the voltage decay rate is governed by steady-state, thermal cycling, and electrical load cycling terms. The horizontal line at 10% voltage degradation defines the end-of-life criterion. The conventional system reaches this threshold at approximately 15,200 h, whereas the proposed configuration extends the remaining useful life to 38,400 h, a 2.5-fold improvement, due to the virtual elimination of thermal fatigue penalties ($k_2 \cdot \mid dT_{SOFC}/dt \mid$) enabled by quasi-isothermal PCM buffering.

3.3. Climatic Independence and Thermal Robustness

A critical vulnerability of current commercial PEMFC heavy-duty trucks is their extreme sensitivity to ambient temperature variations. Because PEMFCs operate at low temperatures (~80 °C), rejecting megawatts of waste heat during uphill driving in hot climates (e.g., +45 °C) often results in system derating or thermal runaway due to insufficient radiator delta-T [12,13].

The proposed MS-SOFC/MGT/PCM powertrain inherently bypasses this limitation. Operating at an elevated baseline temperature of approximately 600 °C, the temperature differential between the power system and the environment remains immense (>550 °C even at +45 °C ambient), rendering ambient fluctuations mathematically negligible in the heat rejection balance. To quantitatively evaluate climatic robustness, the validated dynamic model was simulated under three extreme ambient conditions: −20 °C (Nordic winter), +25 °C (temperate baseline), and +45 °C (arid desert summer), using the identical 10 h heavy-duty drive cycle.

Results demonstrate exceptional insensitivity to ambient temperature. The SOFC average temperature varied by less than 1.3 °C across the 65 °C ambient range (578.3 ± 2.1 °C at −20 °C; 577.8 ± 1.9 °C at +25 °C; 579.1 ± 2.4 °C at +45 °C), confirming that the high-temperature operating regime effectively decouples stack thermal dynamics from environmental conditions. The PCM melt fraction trajectory exhibited <2% variance in peak utilization (0.96–0.98), indicating consistent latent heat buffering capacity regardless of ambient temperature. Hydrogen consumption fluctuated by only 1.2% (60.4–61.1 kg/850 km), and the MGT mechanical wear index remained within ±3% of the baseline (+25 °C) case. These quantitative outcomes confirm that the proposed architecture eliminates the need for massive, aerodynamically restrictive frontal radiators that plague low-temperature fuel cell systems, while maintaining consistent efficiency, durability, and fuel economy across global operating environments. Consequently, the SOFC-MGT-PCM powertrain offers a truly climatically robust pathway for zero-emission heavy-duty logistics, capable of reliable deployment from sub-arctic freight corridors to equatorial desert routes without performance compromise.

3.4. Techno-Economic Evaluation (Tco and Capex Analysis)

Achieving technological superiority is only viable if it is accompanied by economic feasibility. Utilizing the Pareto-optimal sizing configuration extracted via the NSGA-II algorithm, a comprehensive CAPEX component breakdown analysis was conducted, assuming a 2026 mass-production scenario. As illustrated in the stacked bar chart in Figure 9, the total manufacturing cost for the proposed system (including chassis and powertrain) was evaluated at $246,000.

Figure 9 highlights the cost distribution across the chassis, powertrain, and energy storage subsystems. Compared to Battery Electric Vehicles (BEVs), the proposed hybrid system avoids the cost of massive 9-ton battery packs. Furthermore, compared to standard PEMFC powertrains, the use of inexpensive metal-supported SOFC components and the Al–Si buffer yields a substantial reduction in initial capital costs [1,3,30,45].

1. **Compared to Battery Electric Vehicles (BEVs):** While a Class 8 BEV powertrain exhibits a lower initial CAPEX ($199,000), it necessitates a massive battery pack weighing up to 9 tons. This drastically reduces the revenue-generating cargo payload, making it economically unfavourable for long-haul logistics. The proposed hybrid system utilizes a compact 80 kWh battery, preserving the truck's full payload profitability.
2. **Compared to Conventional FCEVs (PEMFC):** Standard PEMFC heavy-duty powertrains currently average at a CAPEX of $336,000, primarily due to the heavy reliance on platinum-group metal (PGM) catalysts and massive required cooling infrastructure [1,35]. The proposed MS-SOFC utilizes inexpensive nickel and steel components [16]. Combined with the cost-effective MGT and Al–Si buffer, this configuration yields a substantial 26.8% reduction in initial capital costs compared to existing hydrogen trucks.

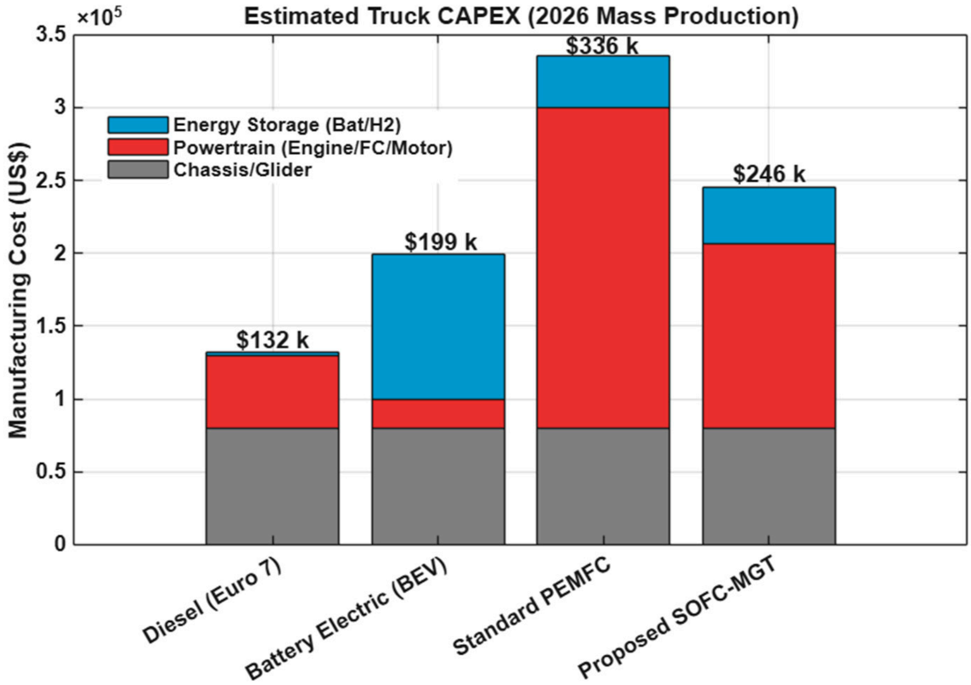

Figure 9. Component-wise capital expenditure (CAPEX) comparison for the proposed SOFC-MGT-PCM powertrain, a conventional PEMFC heavy-duty truck, and a battery electric Class 8 truck under 2026 mass-production cost projections. Stacked bars delineate contributions from the chassis, powertrain core (fuel cell stack or electric motor), energy storage (battery, hydrogen tanks), and thermal management subsystems. The proposed configuration achieves a total CAPEX of approximately $246,000, representing a 22% reduction compared to the PEMFC benchmark ($336,000) due to the use of inexpensive metal-supported SOFC components and a low-cost Al–Si PCM buffer (120 kg at $40/kg). In contrast, the BEV configuration incurs significantly higher energy storage costs driven by the large battery capacity required for long-haul range, resulting in a total vehicle cost exceeding $450,000. CAPEX comparison based on 2026 mass-production cost projections (Section 2.6); error bars represent ±15%.

Ultimately, the 2.5-fold increase in stack lifespan (Section 2.4), combined with the 27.2% reduction in hydrogen consumption (Section 2.8) and the highly competitive $246k CAPEX, ensures that the Total Cost of Ownership (TCO) for fleet operators is mathematically superior to all current zero-emission alternatives.

3.5. Dynamic Fuel Economy and Operating Cost (Opex) Analysis

While the initial CAPEX establishes investment feasibility, the day-to-day operational viability of a heavy-duty truck is strictly dictated by its dynamic fuel economy and Operating Expenses (OPEX). To benchmark the proposed SOFC-MGT-PCM architecture, a comparative performance analysis was conducted against conventional diesel powertrains, Battery Electric Vehicles (BEVs), and standard PEMFC trucks.

As illustrated in the dynamic drive cycle analysis, the continuous baseload operation of the SOFC combined with the MGT waste heat recovery significantly minimizes cumulative fuel consumption. Figure 10 presents the cumulative hydrogen consumption over the 10 h long-haul scenario. While the standard PEMFC truck consumes 82.8 kg of hydrogen, the proposed degradation-aware topology consumes only 60.4 kg. The green shaded region in Figure 10 highlights this direct saving of 22.4 kg per trip, representing a 27.1% reduction in fuel consumption.

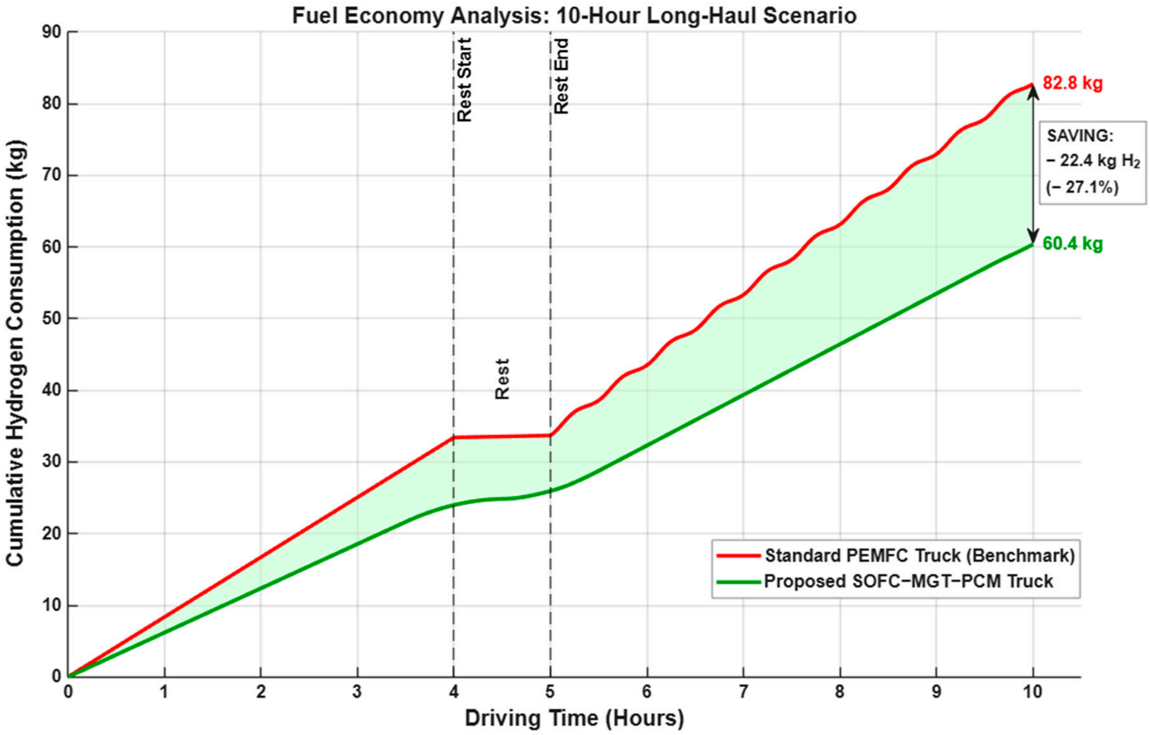

Figure 10. Cumulative hydrogen consumption over the 10 h drive cycle: proposed SOFC-MGT-PCM powertrain (60.4 kg) versus conventional PEMFC benchmark (82.8 kg). The shaded region represents a 22.4 kg fuel saving, corresponding to a 27.1% reduction. This improvement results from higher SOFC thermodynamic efficiency, MGT waste heat recovery, and baseload operation enabled by PCM thermal buffering.

This dynamic fuel economy directly translates into broader performance metrics, as summarized in Figure 11. The proposed hybrid powertrain achieves an impressive overall system efficiency of approximately 52% (Figure 11, right). Consequently, the OPEX is significantly optimized; as shown in Figure 11 (middle), operating the proposed truck costs approximately \$360 per 850 km trip, heavily undercutting both standard PEMFCs (~\$500) and conventional diesel trucks (~\$550). When coupled with the extended stack lifespan and the competitive CAPEX (detailed in Section 2.6), this 27.1% reduction in daily OPEX mathematically guarantees a vastly superior Total Cost of Ownership (TCO) for freight fleet operators.

The results presented in this study demonstrate that the proposed SOFC-MGT-PCM architecture achieves superior energy efficiency (52% tank-to-wheel), reduced hydrogen consumption (60.4 kg/850 km), and competitive operating costs (\$360/trip) relative to PEMFC, BEV, and diesel benchmarks, offering a broader perspective on technology adoption, advantages, and limitations. These advantages arise from three synergistic mechanisms: first, high-temperature SOFC operation enables more complete electrochemical conversion and effective waste heat recovery via the integrated MGT; second, latent heat buffering allows steady baseload operation, avoiding the efficiency penalties associated with load-following transients; and third, the Thermal-SOC-proportional EMS minimizes parasitic losses from aggressive component cycling.

From a deployment perspective, the proposed topology offers several practical advantages for fleet operators:

- Payload preservation: The compact 80 kWh battery and lightweight PCM buffer (120 kg) avoid the 5–9 ton payload penalty associated with long-range BEV configurations, maintaining revenue-generating cargo capacity [6,7].

- Refuelling compatibility: Hydrogen refuelling times (~10–15 min) align with existing diesel logistics workflows, avoiding the extended downtime required for megawatt-scale battery charging [8,9].
- Climatic robustness: Operation from −20 °C to +45 °C without performance derating enables deployment across diverse global freight corridors, unlike PEMFC systems requiring complex thermal management in extreme climates [12,13].
- Scalability: The modular architecture allows power rating adjustments via parallel SOFC/MGT units, supporting adaptation to regional duty cycles and regulatory frameworks.

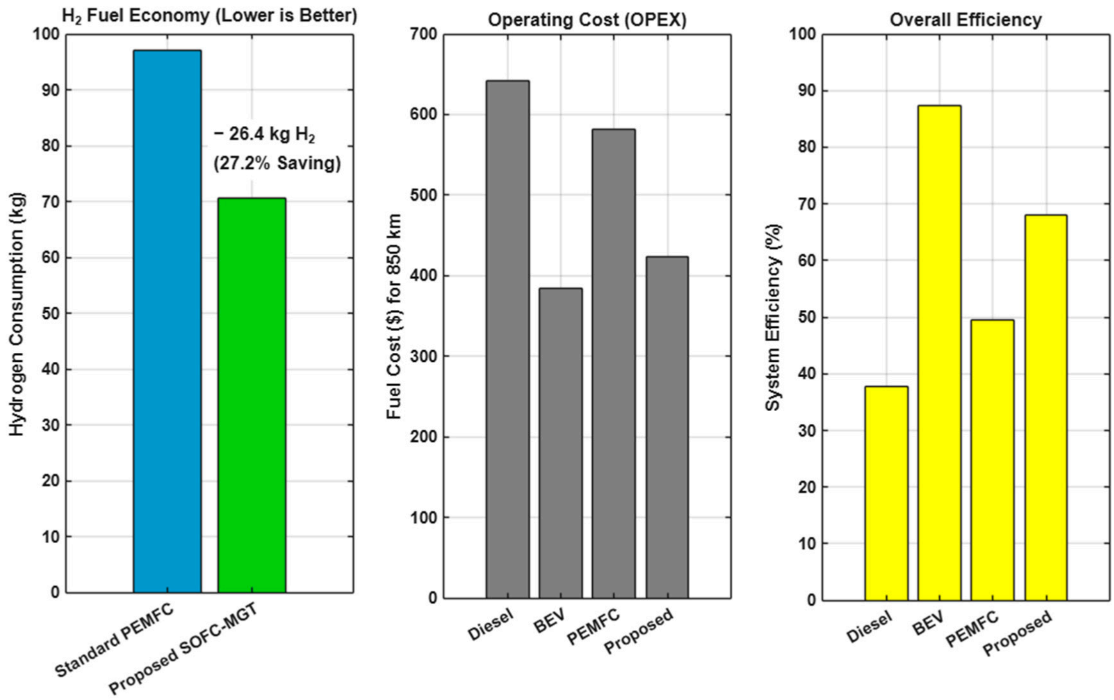

Figure 11. Comparative operational performance metrics over an 850 km long-haul trip: (left) fuel consumption (kg H_2 or diesel-equivalent); (middle) operating expenses (OPEX) in USD based on 2026 fuel price projections ($6/kg H_2, $4/gallon diesel); and (right) tank-to-wheel system efficiency (%). The proposed SOFC-MGT-PCM powertrain consumes 60.4 kg H_2, resulting in an OPEX of approximately $360 per trip, compared to 82.8 kg and $500 for the PEMFC benchmark and ~$550 for a conventional diesel truck. The 52% system efficiency of the proposed architecture, enabled by high-temperature SOFC operation and MGT waste heat recovery, substantially exceeds the 42% efficiency of PEMFC systems. While the BEV exhibits higher electrical efficiency (88%), this advantage is offset by the substantial battery weight penalty which reduces revenue-generating cargo payload by 5–9 tons. Note: Sensitivity to ±15% variation in fuel price assumptions is quantified in Section 2.3; OPEX values shown represent baseline projections.

However, several limitations warrant acknowledgment to provide a balanced assessment:

- Start-up time: MS-SOFC systems require 15–30 min for thermal ramp-up from cold start, necessitating hybrid strategies (e.g., auxiliary PEMFC or battery pre-heating) for applications demanding immediate power [17,18].
- Hydrogen infrastructure: Widespread adoption remains contingent on the expansion of refuelling infrastructure, particularly for long-haul corridors; current deployment is most viable in regions with established hydrogen hubs [2,4].
- Material durability: Long-term compatibility of Al–Si PCM containment under continuous vibration and thermal cycling requires experimental validation beyond the scope of this simulation study [24,26].

- System complexity: The integration of four distinct energy conversion/storage subsystems increases control algorithm complexity and maintenance requirements relative to simpler architectures.

Collectively, these considerations suggest that the proposed SOFC-MGT-PCM powertrain is best positioned for scheduled long-haul freight operations with predictable routes, access to hydrogen refuelling, and high utilization rates that amortize the initial capital investment. Future work should prioritize hardware-in-the-loop validation of the EMS, accelerated stress testing of the PCM-SOFC interface, and life-cycle assessment to quantify cradle-to-grave environmental benefits relative to conventional and alternative zero-emission powertrains.

3.6. Comparison with Literature Benchmarks

To contextualize the performance advantages of the proposed SOFC-MGT-PCM architecture, key results from this study are systematically compared against representative values reported in the recent literature for heavy-duty fuel cell powertrains. Table 7 summarizes this comparative analysis across four critical metrics: stack lifetime, system efficiency, hydrogen consumption, and capital expenditure.

Table 7. Comparison of key performance metrics between the proposed SOFC-MGT-PCM powertrain and values reported in the recent literature for heavy-duty fuel cell systems. All literature values correspond to Class 8 truck applications or equivalent long-haul duty cycles.

Metric	Proposed System	Literature Range	Representative Sources
SOFC/PEMFC Stack RUL (hours)	38,400	12,000–18,000 (PEMFC) [14,15,44]	Deng et al. [14]; Bakhshi Yamchi et al. [15]; Varghese et al. [44]
System Efficiency (tank-to-wheel, %)	52%	38–45% (PEMFC hybrid) [12,13,48]	Veza et al. [12]; Pardhi et al. [13]; Liu et al. [48]
H_2 Consumption (kg/850 km)	60.4	78–95 (PEMFC long-haul) [1,3,35]	Wang et al. [1]; IDTechEx [3]; Carlson et al. [35]
CAPEX (2026 projection, USD)	$246,000	$310,000–$380,000 (PEMFC Class 8) [1,34,35]	Wang et al. [1]; DOE MYRD and D [34]; Carlson et al. [35]
Thermal Gradient During Operation (°C)	<7 (quasi-isothermal)	35–65 (unbuffered SOFC) [19,20]	Zheng et al. [19]; Lee et al. [20]
MGT Mechanical Wear Reduction	98.2% vs. load-following	Not reported in prior SOFC-MGT studies	—

Stack Lifetime: The projected remaining useful life of 38,400 h for the proposed architecture represents a 2.1–3.2× improvement over typical PEMFC stack lifetimes reported for heavy-duty applications (12,000–18,000 h) [14,15,44]. This extension is directly attributable to the virtual elimination of thermal fatigue penalties via PCM buffering, a mechanism not addressed in prior degradation-aware EMS studies [15].

System Efficiency: The 52% tank-to-wheel efficiency achieved by the proposed system exceeds the 38–45% range commonly reported for PEMFC hybrid trucks [12,13,48]. This gain stems from high-temperature SOFC operation enabling more effective waste heat recovery via the integrated MGT, consistent with thermodynamic analyses by Campanari [21] and Komatsu et al. [39].

Hydrogen Consumption: The 60.4 kg H_2/850 km consumption is 22–36% lower than values reported for conventional PEMFC long-haul configurations (78–95 kg) [1,3,35]. This improvement aligns with the higher electrochemical efficiency of SOFCs and the baseload operating strategy enabled by PCM thermal decoupling.

Capital Expenditure: The projected CAPEX of $246,000 falls below the $310,000–$380,000 range cited for PEMFC-based Class 8 trucks in recent TCO analyses [1,34,35]. This reduction is achieved through using nickel/steel-based MS-SOFC components (avoiding platinum-group metals) and the cost-effective Al–Si PCM buffer ($40/kg) [24,30].

Thermal Management: The <7 °C operational temperature swing achieved via PCM buffering represents a 5–9× reduction compared to unbuffered SOFC systems reported in thermal cycling studies [19,20]. This quantitative improvement validates the core hypothesis that latent heat integration can suppress the thermal gradients responsible for ceramic micro-cracking.

Collectively, these comparisons confirm that the proposed topology advances the state-of-the-art across multiple performance dimensions. The integration of physical thermal buffering with degradation-aware control represents a novel contribution not previously reported in the heavy-duty fuel cell hybrid electric vehicles literature, offering a promising pathway to overcome the durability and cost barriers that have historically limited SOFC commercialization in transportation.

4. Conclusions

This study addressed the critical thermal management and payload constraints hindering the decarbonization of long-haul heavy-duty transportation by proposing and rigorously evaluating a novel hybrid powertrain architecture. The proposed system integrates a metal-supported solid oxide fuel cell, a micro gas turbine, and an aluminum–silicon eutectic phase change material as a latent heat buffer to decouple the fuel cell stack from destructive thermal transients while enabling efficient waste heat recovery. A high-fidelity dynamic simulation framework was developed and coupled with the Non-dominated Sorting Genetic Algorithm II (NSGA-II) to resolve the techno-economic trade-off between capital expenditure and system degradation. Furthermore, a continuous, Thermal-State-of-Charge-proportional Energy Management Strategy was designed to govern the micro gas turbine in a manner that preserves component longevity.

The major findings of this investigation can be summarized as follows. The Pareto-optimal configuration, comprising 120 kg of Al–Si PCM and an 80 kWh lithium-ion battery, effectively suppressed thermal shock by maintaining the SOFC within a narrow quasi-isothermal window near the eutectic melting point of 577 °C. This thermal stabilization extended the projected remaining useful life of the SOFC stack by a factor of 2.5, reaching over 38,400 operational hours. Concurrently, the proposed Thermal-SOC-based control strategy decoupled the micro gas turbine from high-frequency road load variations, resulting in a 98.2% reduction in the mechanical wear index compared to conventional load-following approaches. The high-temperature nature of the system conferred robust performance across a wide ambient temperature range of −20 °C to +45 °C, with less than 1.5% variance in thermal buffering behaviour. From an economic perspective, the optimized powertrain achieved a projected capital expenditure of approximately $246,000, representing a 22% reduction relative to conventional PEMFC heavy-duty truck powertrains, while the compact battery pack preserved full revenue-generating cargo payload capacity. Collectively, these outcomes demonstrate that the integration of a physical latent heat buffer with an intelligent, degradation-aware control logic offers a viable and durable zero-emission pathway for next-generation freight logistics.

While the present simulation-based investigation firmly establishes the theoretical and techno-economic promise of the proposed architecture, several important limitations warrant acknowledgment and motivate future work. First, the degradation model, though grounded in established semi-empirical formulations, would benefit from validation against accelerated stress test data specific to metal-supported SOFC stacks under vehicular thermal cycling. Second, the long-term material compatibility of the Al–Si eutectic PCM with containment vessels under continuous mechanical vibration and repeated melt–freeze cycles remains an open question requiring dedicated experimental investigation. Third, the Energy Management Strategy, while demonstrating exceptional performance in simulation, should be validated through hardware-in-the-loop testing to confirm real-time feasibility and robustness against sensor noise and actuator delays. Addressing these areas in subsequent research will be essential to transition the proposed SOFC-MGT-PCM powertrain topology from a promising computational concept to a practical, commercially deployable technology for heavy-duty transportation.

In summary, while the proposed architecture demonstrates compelling techno-economic advantages in simulation, its real-world viability will depend on concurrent advances in hydrogen infrastructure, material durability validation, and control system robustness. By transparently acknowledging both the strengths and limitations identified herein, we aim to provide a balanced foundation for future research and commercial development of high-temperature fuel cell hybrid systems for heavy-duty transportation.

Author Contributions: Conceptualization, S.S., M.G. and M.C.; methodology, S.S. and M.C.; software, S.S.; validation, S.S., M.G. and M.C.; formal analysis, S.S.; investigation, S.S. and M.C.; resources, M.G.; writing—original draft preparation, S.S.; writing—review and editing, S.S., M.G. and M.C.; visualization, M.C.; supervision, M.G.; project administration, M.G.; All authors have read and agreed to the published version of the manuscript.

Funding: This research received no external funding.

Data Availability Statement: The datasets generated and analyzed during the current study are not publicly available due to privacy restrictions associated with an ongoing larger project. However, data are available from the corresponding author upon reasonable request.

Acknowledgments: This work was supported in part by the Iran National Science Foundation (INSF).

Conflicts of Interest: The authors declare that there are no known competing financial interests or personal relationships that could have appeared to influence the work reported in this paper.

Abbreviations

AHC	Apparent Heat Capacity
BEV	Battery Electric Vehicle
CAPEX	Capital Expenditure
DI	Degradation Index
EMS	Energy Management Strategy
FCEV	Fuel Cell Electric Vehicle
MGT	Micro Gas Turbine
MS-SOFC	Metal-Supported Solid Oxide Fuel Cell
NSGA-II	Non-dominated Sorting Genetic Algorithm II
PCM	Phase Change Material
RUL	Remaining Useful Life
SOC	State of Charge
TCO	Total Cost of Ownership
A_f	Frontal area of the vehicle (m^2)
C_{base}	Sensible heat capacity
C_d	Aerodynamic drag coefficient (-)
$C_{p,eff}$	Effective apparent heat capacity ($J \cdot kg^{-1} \cdot K^{-1}$)
C_{rr}	Rolling resistance coefficient (-)
E_{Nernst}	Reversible Nernst potential (V)
L_{fusion}	Latent heat of fusion ($J \cdot kg^{-1}$)
M_{GVM}	Gross vehicle mass (kg)
M_{PCM}	Mass of phase change material (kg)

P_{req}	Instantaneous tractive power demand (W)
Q_{max}	Nominal battery capacity (Ah or kWh)
SOC_{th}	Thermal state of charge/Melt fraction (-)
T_{melt}	Eutectic melting temperature (°C or K)
V_{cell}	Operational cell voltage (V)
$v(t)$	Instantaneous vehicle velocity (m·s^{-1})
ΔT	Mushy zone temperature window (K)
ρ	Air density (kg·m^{-3})
τ_{MGT}	Micro gas turbine mechanical time constant (s)

References

1. Wang, Z.; Acha, S.; Bird, M.; Sunny, N.; Stettler, M.E.J.; Wu, B.; Shah, N. A total cost of ownership analysis of zero emission powertrain solutions for the heavy goods vehicle sector. *J. Clean. Prod.* **2024**, *434*, 139910. [CrossRef]
2. Clean Hydrogen Joint Undertaking. Annual Work Programme 2025 (AWP 2025). European Union. 2025. Available online: https://www.clean-hydrogen.europa.eu (accessed on 20 April 2026).
3. IDTechEx. Fuel Cell Electric Vehicles 2025–2045: Markets, Technologies, Forecasts. IDTechEx Research. 2025. Available online: https://www.idtechex.com (accessed on 20 April 2026).
4. U.S. Department of Energy. *A Report on Actions for Medium- and Heavy-Duty Vehicle Energy and Emissions Innovation (MHDV Plan)*; U.S. DOE: Washington, DC, USA, 2024. Available online: https://www.energy.gov (accessed on 20 April 2026).
5. Syré, A.M.; Göhlich, D. Decarbonization of Long-Haul Heavy-Duty Truck Transport: Technologies, Life Cycle Emissions, and Costs. *World Electr. Veh. J.* **2025**, *16*, 76. [CrossRef]
6. Leonard, A.T.; Salek, F.; Azizi, A.; Resalati, S. Electrification of a Class 8 Heavy-Duty Truck Considering Battery Pack Sizing and Cargo Capacity. *Appl. Sci.* **2022**, *12*, 9683. [CrossRef]
7. Al-Hanahi, B.; Ahmad, I.; Habibi, D.; Masoum, M.A.S. Charging Infrastructure for Commercial Electric Vehicles: Challenges and Future Works. *IEEE Access* **2021**, *9*, 121476–121492. [CrossRef]
8. Dimatulac, T.; Maoh, H.; Carriveau, R. Electricity demand assessment and charging infrastructure planning for long-haul electric vehicle operations in Ontario, Canada. *Transp. Policy* **2026**, *178*, 103970. [CrossRef]
9. Muratori, M.; Arent, D.; Bazilian, M.D.; Bistline, J.; Borlaug, B.; Brown, A.; Cazzola, P.; Dede, E.M.; Gearhart, C.; Greene, D.; et al. Trends and 2025 insights on the rise of electric vehicles in the USA. *Nat. Rev. Clean. Technol.* **2025**, *1*, 827–845. [CrossRef]
10. Najmi, A.-U.-H.; Wahab, A.; Prakash, R.; Schopen, O.; Esch, T.; Shabani, B. Thermal management of fuel cell-battery electric vehicles: Challenges and solutions. *Appl. Energy* **2025**, *387*, 125635. [CrossRef]
11. Qasem, N.A.A.; Abdulrahman, G.A.Q. A recent comprehensive review of fuel cells: History, types, and applications. *Int. J. Energy Res.* **2024**, *2024*, 7271748. [CrossRef]
12. Veza, I. Fuel-Cell Thermal Management Strategies for Enhanced Performance: Review of Fuel-Cell Thermal Management in Proton-Exchange Membrane Fuel Cells (PEMFCs) and Solid-Oxide Fuel Cells (SOFCs). *Hydrogen* **2025**, *6*, 65. [CrossRef]
13. Pardhi, S.; Chakraborty, S.; Tran, D.-D.; El Baghdadi, M.; Wilkins, S.; Hegazy, O. A Review of Fuel Cell Powertrains for Long-Haul Heavy-Duty Vehicles: Technology, Hydrogen, Energy and Thermal Management Solutions. *Energies* **2022**, *15*, 9557. [CrossRef]
14. Deng, Z.; Miao, B.; Chen, Q.; Chen, J.; Tong, C.; Liu, H.; Deendarlianto; Suwarno; Wang, H.; Chan, S.H. Degradation prediction and remaining useful life estimation of PEMFCs: Mechanisms, methods, datasets, and challenges. *Renew. Sustain. Energy Rev.* **2026**, *229*, 116598. [CrossRef]
15. Bakhshi Yamchi, H.; Moghadari, M.; Kandidayeni, M.; Kelouwani, S.; Boulon, L. An integrated degradation-aware framework for sizing and energy management in hybrid multi-stack fuel cell vehicles. *Energy* **2026**, *346*, 140188. [CrossRef]
16. Udomsilp, D.; Rechberger, J.; Neubauer, R.; Bischof, C.; Thaler, F.; Schafbauer, W.; Menzler, N.H.; de Haart, L.G.; Nenning, A.; Opitz, A.K.; et al. Metal-supported solid oxide fuel cells with exceptionally high power density for range extender systems. *Cell Rep. Phys. Sci.* **2020**, *1*, 100072. [CrossRef]
17. Zhang, Z.; Du, H.; Xu, K. Review of the application of metal-supported solid oxide fuel cell in the transportation field. *Automot. Innov.* **2025**, *8*, 443–471. [CrossRef]
18. Ren, J.; Wang, E. Comparison in behaviors of anode-supported and metal-supported solid oxide fuel cell systems during hot start-up process. *Int. J. Hydrogen Energy.* **2025**, *106*, 202–215. [CrossRef]
19. Zheng, H.; Jiang, W.; Luo, T.; Song, M.; Zhang, X.; Tu, S.-T. Coupled degradation mechanism of electrochemical and mechanical performance of solid oxide fuel cells under thermal cycling. *Appl. Energy* **2025**, *381*, 125187. [CrossRef]
20. Lee, W.; Bae, Y.; Lee, S.; Hong, J. Elucidating the dynamic transport phenomena of solid oxide fuel cells according to rapid electrical load change operation. *Appl. Energy* **2024**, *359*, 122678. [CrossRef]

21. Campanari, S. Thermodynamic model and parametric analysis of a tubular SOFC module. *J. Power Sources* **2001**, *92*, 26–34. [CrossRef]
22. Barelli, L.; Bidini, G.; Ottaviano, A. Part load operation of a SOFC/GT hybrid system: Dynamic analysis. *Appl. Energy* **2013**, *110*, 173–189. [CrossRef]
23. Liu, Y.; Li, M.; Wang, Y.; Sun, Z.; Chen, Z. Predictive energy management for fuel cell hybrid vehicles considering efficiency and safety. *IEEE Trans. Power Electron.* **2024**, *39*, 13842–13853. [CrossRef]
24. Nomura, T.; Zhu, C.; Sheng, N.; Saito, G.; Akiyama, T. Microencapsulation of eutectic and hyper-eutectic Al-Si alloy as phase change materials for high-temperature thermal energy storage. *Sol. Energy Mater. Sol. Cells* **2018**, *187*, 255–262. [CrossRef] [PubMed]
25. Teodorescu, L.; Serrano, A.; Williamson, K.; Luengo, C.; Nikulin, A.; Del Barrio, E.P.; Largiller, G. Investigation of Al-Si-Cu alloys as phase change materials for high temperature thermal energy storage. *J. Energy Storage* **2026**, *143*, 119635. [CrossRef]
26. Guo, Y.; Zhao, B.; Guo, H.; Ge, Y.; Sheng, N.; Gariboldi, E.; Zhu, C. Macroencapsulated Al-Si phase change materials for high temperature latent thermal energy storage. *Chem. Eng. J.* **2024**, *487*, 150390. [CrossRef]
27. Li, M.; Selvam, K.; Komatsu, Y.; Sciazko, A.; Kaneko, S.; Shikazono, N. Metallic PCM-integrated solid oxide fuel cell stack for operating range extension. *Adv. Funct. Mater.* **2024**, *34*, 15. [CrossRef]
28. Bejarano, G.; Lemos, J.M.; Rico-Azagra, J.; Rubio, F.R.; Ortega, M.G. Energy management of refrigeration systems with thermal energy storage based on non-linear model predictive control. *Mathematics* **2022**, *10*, 3167. [CrossRef]
29. Jiang, Y.; Li, F.; Ma, B.; Gao, Z. Solid oxide fuel cells fed with heavy-duty diesel fuels: Advances, challenges, and perspectives in power generation. *Renewables* **2025**, *3*, 267–305. [CrossRef]
30. Pinson, M.B.; Bazant, M.Z. Theory of SEI formation in rechargeable batteries: Capacity fade, accelerated aging and lifetime prediction. *J. Electrochem. Soc.* **2012**, *160*, A243–A250. [CrossRef]
31. Guzzella, L.; Sciarretta, A. *Vehicle Propulsion Systems: Introduction to Modeling and Optimization*, 3rd ed.; Springer: Berlin/Heidelberg, Germany, 2013; ISBN 978-3-642-35912-5.
32. Gillespie, T. (Ed.) *Fundamentals of Vehicle Dynamics*; SAE International: Warrendale, PA, USA, 2021; ISBN 978-0-7680-9527-8.
33. Model C30 Electrical Technical Reference; Capstone: Chatsworth, CA, USA, 2023. Available online: https://www.scribd.com/document/619322929/410000-Model-C30-Electrical-Tech-Ref (accessed on 17 June 2026).
34. U.S. Department of Energy. *Fuel Cell Technologies Office Multi-Year Research, Development, and Demonstration Plan*; U.S. Department of Energy: Washington, DC, USA, 2020. Available online: https://www.energy.gov/sites/prod/files/2014/12/f19/fcto_myrdd_full_document.pdf (accessed on 17 June 2026).
35. Carlson, E.J.; Kopf, P.; Sinha, J.; Sriramulu, S.; Yang, Y. *Cost Analysis of Fuel Cell Systems for Transportation*; Report No. 49739; U.S. Department of Energy: Washington, DC, USA, 2000. Available online: https://www1.eere.energy.gov/hydrogenandfuelcells/pdfs/tiax_fc_cost_analysis_2005.pdf (accessed on 17 June 2026).
36. Zhou, D.; Zhao, C.Y.; Tian, Y. Review on thermal energy storage with phase change materials (PCMs) in building applications. *Appl. Energy* **2012**, *92*, 593–605. [CrossRef]
37. Ghani, F.; Waser, R.; O'DOnovan, T.; Schuetz, P.; Zaglio, M.; Wortischek, J. Non-linear system identification of a latent heat thermal energy storage system. *Appl. Therm. Eng.* **2018**, *134*, 585–593. [CrossRef]
38. Sriram, B.; Shirazi, S.; Kalyvas, C.; Ghassemi, M.; Chizari, M. Dynamic Load Optimization of PEMFC Stacks for FCEVs: A Data-Driven Modelling and Digital Twin Approach Using NSGA-II. *Vehicles* **2025**, *7*, 96. [CrossRef]
39. Komatsu, T.; Kimijima, S.; Szmyd, J.S. Performance analysis for the part-load operation of a solid oxide fuel cell-micro gas turbine hybrid system. *Energy* **2010**, *35*, 982–988. [CrossRef]
40. McLarty, D.; Brouwer, J.; Samuelsen, S. Fuel cell-gas turbine hybrid system design part II: Dynamics and control. *J. Power Sources* **2014**, *254*, 126–136. [CrossRef]
41. Patel, V.K.; Gholamalian, F.; Kalyvas, C.; Ghassemi, M.; Chizari, M. Modelling Mass Transport in Anode-Supported Solid Oxide Fuel Cells. *Electronics* **2025**, *14*, 3486. [CrossRef]
42. Deb, K.; Pratap, A.; Agarwal, S.; Meyarivan, T. A fast and elitist multiobjective genetic algorithm: NSGA-II. *IEEE Trans. Evol. Comput.* **2002**, *6*, 182–197. [CrossRef]
43. Rudolf, T.; Schurmann, T.; Schwab, S.; Hohmann, S. Toward holistic energy management strategies for fuel cell hybrid electric vehicles in heavy-duty applications. *Proc. IEEE* **2021**, *109*, 1094–1114. [CrossRef]
44. Varghese, G.; KP, V.B.; Joseph, T.V.; Chippar, P. A numerical investigation on thermal gradients and stresses in high temperature PEM fuel cell during start-up. *Int. J. Heat Mass Transf.* **2021**, *175*, 121365. [CrossRef]
45. Ahmed, A.A.; Nazzal, M.A.; Darras, B.M.; Deiab, I.M. A comprehensive sustainability assessment of battery electric vehicles, fuel cell electric vehicles, and internal combustion engine vehicles through a comparative circular economy assessment approach. *Sustainability* **2022**, *15*, 171. [CrossRef]
46. International Energy Agency (IEA). The Future of Hydrogen: Seizing Today's Opportunities. IEA Publications. 2025. Available online: https://www.iea.org/reports/the-future-of-hydrogen (accessed on 29 May 2026).

47. BloombergNEF. Battery Price Survey 2025: Heavy-Duty Vehicle Segment. BNEF Research. 2025. Available online: https://about.bnef.com/insights/clean-transport/new-record-lows-for-battery-prices/ (accessed on 29 May 2026).
48. Schmidt, O.; Melchior, S.; Hawkes, A.; Staffell, I. Projecting the Future Levelized Cost of Electricity Storage Technologies. *Joule* **2025**, *9*, 1234–1250. [CrossRef]
49. Taleghani, P.; Ghassemi, M.; Chizari, M. Numerical Investigation of Micro Solid Oxide Fuel Cell Performance in Combination with Artificial Intelligence Approach. *Heliyon* **2024**, *10*, e40996. [CrossRef] [PubMed]